Research Square

Preprints are preliminary reports that have not undergone peer review.
They should not be considered conclusive, used to inform clinical practice,
or referenced by the media as validated information.

Comprehensive Analysis of SHC1 Expression and Its Role in Glioblastoma Progression and Immune Modulation

Yi Xu
Nanchang University
Jianghua Zhu
Nanchang University
Min Luo
Nanchang University
Li Guo
Nanchang University
Xinyue Wei
Nanchang University
Xingen Zhu
Nanchang University
Kunjian Lei
kunjian.lei@ncu.edu.cn
Nanchang University

Research Article

Keywords:

Posted Date: November 9th, 2026

DOI: https://doi.org/10.21203/rs.3.rs-11382820/v1

License: This work is licensed under a Creative Commons Attribution 4.0 International License.
Read Full License

Additional Declarations: No competing interests reported.

Comprehensive Analysis of SHC1 Expression and Its Role in Glioblastoma Progression and Immune Modulation

Yi Xu[1,2,3,4], Jianghua Zhu[1,2,3,4], Min Luo[1,2,3,4], Li Guo[1], Xinyue Wei[5], Xingen Zhu[1,2,3,4,5]*, Kunjian Lei[1,2,3,4,5]*

[1]Department of Neurosurgery, The Second Affiliated Hospital, Jiangxi Medical College, Nanchang University, Nanchang, Jiangxi, P. R. China.

[2]Jiangxi Province Key Laboratory of Neurological Diseases, Nanchang, Jiangxi, P. R. China.

[3]JXHC Key Laboratory of Neurological Medicine, Nanchang University, Nanchang, Jiangxi, China.

[4]The MOE Basic Research and Innovation Center for the Targeted Therapeutics of Solid Tumors, Jiangxi Medical College, Nanchang University, Nanchang, Jiangxi, China.

[5]School of Basic Medical Sciences, Nanchang University, Nanchang, P. R. China.

***Correspondence:**

Kunjian Lei

kunjian.lei@ncu.edu.cn

Xingen Zhu

ndefy89006@ncu.edu.cn

Abstract:

SHC adaptor protein 1 (SHC1) encodes three protein isoforms, including p66Shc, a well-characterized mediator of oxidative stress responses. Despite evidence implicating SHC1 in tumorigenesis and progression, its pan-cancer expression landscape and functional significance in glioblastoma (GBM) remain incompletely characterized. Herein, we integrated multi-omics datasets from The Cancer Genome Atlas (TCGA), the Genotype-Tissue Expression (GTEx) project, and the Clinical Proteomic Tumor Analysis Consortium (CPTAC) to comprehensively characterize SHC1 expression patterns, prognostic relevance, and associations with the immune landscape across 33 cancer types. Our analysis showed significant SHC1 upregulation in several malignancies, including GBM, which correlated with unfavorable prognosis and immunosuppressive cell infiltration. Functional assays further showed that silencing SHC1 in GBM cells significantly impaired proliferative, migratory, and invasive capacities, accompanied by G_2/M cell-cycle arrest, increased apoptosis, and enhanced responsiveness to temozolomide (TMZ). Integrative transcriptomic and proteomic analyses identified CCNB1 as a key downstream effector mediating SHC1-driven cell cycle progression; restoration of CCNB1 partially reversed the phenotypic effects of SHC1 loss. In vivo experiments further demonstrated that SHC1 silencing restrained intracranial tumor progression and extended survival in both immunodeficient and immunocompetent mouse models. Single-cell RNA sequencing also indicated a reshaped tumor immune microenvironment, characterized by reduced immunosuppressive macrophages and increased $CD8^+$ T cell infiltration. Collectively, these results identify SHC1 as a multifaceted contributor to GBM malignancy by

supporting proliferation, DNA repair, and immune escape, underscoring its potential as both a therapeutic target and a prognostic biomarker in GBM.

INTRODUCTION

Cancer remains a substantial burden on global public health and socioeconomic development in the 21st century [1]. Globally, it accounts for approximately 16.8% of all deaths and 22.8% of mortality attributable to non-communicable diseases [2]. Cancer contributes significantly to premature mortality from noncommunicable diseases (NCDs), accounting for 30.3% of deaths among individuals aged 30–69 years. Cancer remains one of the top three leading causes of mortality in this age group across 177 of 183 countries, demonstrating its significant global health burden [2]. Current treatment strategies, including surgery, radiotherapy, chemotherapy, immunotherapy, and molecular targeted therapy, exhibit limited efficacy in achieving long-term survival for many patients [3,4]. Therefore, identifying novel biomarkers, improving prognostic stratification tools and discovering actionable therapeutic targets are essential for precision oncology and sustained antitumor responses.

SHC adaptor protein 1 (SHC1) encodes the ShcA adaptor protein, which is expressed as three principal isoforms: p46Shc, p52Shc, and p66Shc [5]. Among these, p66Shc is the largest isoform and uniquely harbors a collagen homology 2 (CH2) domain that critically regulates mitochondrial reactive oxygen species (ROS) generation and apoptosis [6]. ShcA expression is dynamically regulated in the central nervous system, with high abundance in proliferating neural progenitors and a

pronounced decrease upon differentiation [7,8]. Functionally, ShcA adaptor proteins integrate diverse signaling pathways to mediate cellular responses to extracellular stimuli [9–11]. Unlike other ShcA isoforms, p66Shc plays a distinct role in oxidative stress responses and exerts context-dependent effects in cancer, favoring apoptosis or cell survival depending on cell type, growth factor signaling, and microenvironmental stress [12–14].

Dysregulated p66Shc expression and altered p66Shc-mediated signaling are implicated in diverse pathological conditions, particularly malignancies. Increased p66Shc expression is linked to tumor cell proliferation, migration, and tumorigenesis. Upon EGF stimulation, p66Shc and Grb2 form a complex with the small GTPases ARF1 and ARF6, which in turn facilitates breast cancer cell proliferation, invasion, and migration [15,16]. In prostate cancer, ROS production driven by p66Shc, along with subsequent Rac1 activation, suppresses cPAcP, a prostate-specific phosphatase sharing functional homology with PTEN, thereby promoting tumor cell growth and survival. [17,18]. p66Shc is also highly expressed in colorectal and gastric cancers. In this context, it enhances colorectal tumor cell survival by activating the PI3K/AKT pathway [19,20]. In hepatocellular carcinoma, p66Shc promotes tumor progression by phosphorylating STAT3 and activating downstream growth-promoting signaling [21,22]. Notably, among SHC1 isoforms, p66Shc alone has been reported to be markedly elevated in glioblastoma (GBM) and linked to unfavorable patient prognosis [23]. However, in contrast to the extensive investigation of SHC1 in cancers such as breast and lung malignancies, its functions and underlying mechanisms in GBM remain

incompletely characterized. Despite accumulating evidence for p66Shc across individual cancer types, a comprehensive pan-cancer assessment of SHC1 expression patterns, prognostic significance, and immune associations remains lacking. Furthermore, whether aberrant SHC1 expression drives GBM progression through specific signaling pathways and whether SHC1 is functionally linked to the tumor immune microenvironment remain unclear. Therefore, a comprehensive dissection of the biological functions and regulatory circuitry orchestrated by SHC1 in GBM could shed light on its mechanistic role in driving malignancy and emphasize its value as a therapeutic candidate and prognostic indicator.

Our initial analysis leveraged public multi-omics resources to profile SHC1 expression, prognostic relevance, and associations with immune cell infiltration across multiple tumor types, followed by an in-depth investigation in GBM. Subsequently, bioinformatic approaches were integrated with in vitro functional assays and in vivo xenograft and syngeneic models to determine the impact of SHC1 silencing on GBM cell proliferation, migration, invasion, cell-cycle progression, and apoptosis. The effects of SHC1 loss on chemosensitivity and the tumor immune microenvironment were also examined. Through this multilevel and multimodel strategy, the functional relevance and mechanistic underpinnings of SHC1 in GBM were defined, alongside an evaluation of its prognostic and therapeutic potential.

RESULTS

Expression of SHC1 in Pan-Cancer Studies

The *SHC1* gene encodes three distinct protein isoforms (p46Shc, p52Shc, and p66Shc) harboring diverse protein–lipid and protein–protein interaction domains that enable distinct functional properties [24]. Although SHC1 has emerged as a potential regulator of tumorigenesis and cancer progression, its pan-cancer landscape remains incompletely characterized. To address this, TCGA and GTEx datasets were integrated to evaluate SHC1 mRNA expression across tumor and corresponding non-cancerous tissues. Among the 33 cancer types examined, SHC1 exhibited significantly increased expression in 14 tumors and significantly decreased expression in 12 tumors compared with corresponding non-cancerous tissues (Fig. 1A). Clinical Proteomic Tumor Analysis Consortium (CPTAC) analysis further showed increased SHC1 protein abundance in five tumor types but decreased abundance in UCEC (Fig. S1A). Notably, SHC1 was significantly upregulated in GBM at both the transcriptional and protein levels (Fig. 1B, C). Analysis of cBioPortal data revealed that SHC1 alterations were most prevalent in Cholangiocarcinoma (CHOL) (14%), predominantly driven by amplification (Fig. 1D). The Human Protein Atlas (HPA) immunofluorescence showed mainly cytoplasmic localization of SHC1 in U2OS and U251MG cells (Fig. 1E). STRING-based protein–protein interaction analysis indicated that SHC1-interacting proteins were mainly localized to the cytoplasm, plasma membrane, mitochondria, and nucleus (Fig. 1F).

Prognostic Value of SHC1 in Pan-Cancer

The prognostic significance of SHC1 was then assessed using four survival endpoints: overall survival (OS), progression-free interval (PFI), disease-free interval (DFI), and

disease-specific survival (DSS) (Fig. 2A). Across cancers, SHC1 demonstrated a protective role only in PCPG based on DFI and PFI, whereas it acted as a risk factor in more than ten tumor types, including brain lower-grade glioma (LGG), uveal melanoma (UVM), and lung adenocarcinoma (LUAD). Notably, in GBM, lung squamous cell carcinoma (LUSC), prostate adenocarcinoma (PRAD), and rectum adenocarcinoma (READ), SHC1 showed significant associations with DSS rather than OS, suggesting that its prognostic relevance may be more closely related to disease-specific progression or recurrence than to all-cause survival in these tumors. Univariate Cox regression across 33 TCGA cancer types further supported the prognostic role of SHC1 (Fig. 2B): Elevated SHC1 levels significantly predicted worse survival in LGG, UVM, LUAD, KIRP, and multiple other cancers. Kaplan–Meier analysis based on the optimal cutoff similarly demonstrated poorer outcomes in patients with high SHC1 expression in GBM, LGG, PAAD, and MESO (Fig. 2C–F). In GBM specifically, SHC1 expression was not significantly associated with OS when stratified by median expression; however, when the optimal cutoff was applied, patients with higher SHC1 expression exhibited significantly shorter survival (Fig. S1B). In contrast, DSS remained significantly associated with SHC1 expression regardless of whether median or optimal cutoff thresholds were used, with high SHC1 expression associated with longer DSS (Fig. S1B).

Immune Landscape of SHC1 Across Cancers and Gene Set Enrichment Analysis (GSEA)

TISCH-based single-cell profiling indicated that SHC1 expression was largely

restricted to malignant cells across most cancers, with minimal presence in immune populations (Fig. S2A). Representative scRNA-seq datasets from glioma and leiomyosarcoma further confirmed that cells with high SHC1 expression were enriched mainly within malignant-cell populations rather than immune-cell compartments (Fig. 3A, S2B). Pan-cancer analysis via the TIMER 3.0 database revealed that SHC1 expression positively correlated with infiltrating macrophages, neutrophils, and Tregs, but negatively correlated with B cells and $CD8^+$ T cells across multiple malignancies (Fig. S3), suggesting its widespread role in modulating the immune microenvironment.

In GBM, single-sample GSEA (ssGSEA) revealed that elevated SHC1 expression correlated with reduced tumor purity and elevated ESTIMATE, Immune, and Stromal Scores, along with increased infiltration of most immune cell types. Immune infiltration was particularly prominent in mesenchymal GBM, likely due to bidirectional crosstalk between neoplastic cells and the immune microenvironment [25]. Specifically, SHC1 expression correlated positively with neutrophils, macrophages, and $CD4^+$ T cells. Although these immune populations are heterogeneous, multiple studies have indicated that they often acquire immunosuppressive or oncogenic phenotypes within GBM rather than mediating effective antitumor immunity [26,27]. Accordingly, high SHC1 expression may contribute not only to tumor-intrinsic malignant behavior but also to establishing a suppressive GBM immune milieu. However, the specific mechanisms through which SHC1 regulates immune cell recruitment and functional polarization require further experimental validation.

GSEA of Hallmark gene sets was performed on each cancer type stratified by

SHC1 expression levels. Across most tumors, the differentially enriched pathways converged predominantly on IL6_JAK_STAT3_SIGNALING, EPITHELIAL_MESENCHYMAL_TRANSITION, KRAS_SIGNALING, INFLAMMATORY_RESPONSE, and TNFA_SIGNALING_VIA_NFKB (Fig. S4), suggesting that SHC1 is broadly associated with inflammation-driven signaling and EMT across malignancies.

Knocking down SHC1 significantly inhibits GBM progression

To investigate the functional contribution of SHC1 to GBM malignancy, SHC1 was knocked down in human LN229 and U251MG cells, alongside murine Shc1 in GL261 cells. Knockdown efficiency was subsequently verified by qPCR and Western blot (Fig. 4A, S5A, B). Functional assessment via CCK-8 and colony-formation assays revealed that SHC1 depletion markedly impaired proliferative capacity. (Fig. 4B, C, S5C, D). Consistently, EdU incorporation was markedly decreased after SHC1 knockdown, confirming a reduction in the proliferating cell fraction (Fig. 4D, S5E). Wound-healing assays demonstrated impaired migration (Fig. 4E, S5F), while Transwell assays indicated substantial reductions in both migration and invasion. Flow cytometry also detected a significant increase in apoptosis and G_2/M accumulation, indicating cell-cycle arrest at the G_2/M transition (Fig. 4F, G). Thus, SHC1 supports multiple malignant phenotypes in GBM cells, including proliferation, survival, migration, invasion, and cell-cycle progression. Of the three cell lines tested, U251MG exhibited the greatest sensitivity to SHC1 depletion, suggesting a relatively stronger reliance on SHC1 function in this cellular context.

To determine whether SHC1 exerts a growth-promoting effect in vivo, U251MG-Luc cells stably expressing shVector or shSHC1 were orthotopically implanted into the brains of immunodeficient NCG mice. In vivo Imaging System (IVIS) imaging revealed a marked reduction in intracranial bioluminescence upon SHC1 suppression compared with the control group (Fig. 4H, I). Given the absence of functional adaptive immunity in this model, these findings indicate that SHC1 downregulation can directly impede GBM growth through tumor-intrinsic mechanisms, independent of immune-mediated effects. Consistently, immunohistochemical (IHC) staining demonstrated a marked decline in the percentage of Ki-67$^+$ cells following SHC1 knockdown, further substantiating its ability to suppress proliferation in vivo (Fig. 4J).

SHC1 is significantly associated with the cell cycle and TMZ resistance in GBM cells

RNA-seq of SHC1-knockdown U251MG cells identified 720 upregulated and 902 downregulated genes (Fig. 5A), including marked reductions in *SHC1*, *PRC1*, *MYC*, and *CCNB1* (Fig. 5B). GSEA identified marked enrichment changes in cell cycle pathways, including Cell cycle and Cellular senescence, along with several DNA repair pathways such as DNA replication and Fanconi anemia (Fig. 5C). Among the top five pathways downregulated in shSHC1 cells were CELL_CYCLE and DNA_REPLICATION (Fig. S6B), reflecting impaired cell-cycle progression and DNA replication dynamics.

GSEA of proteomic data consistently identified CELL_CYCLE and

DNA_REPLICATION as the top two most affected pathways, consistent with the transcriptomic results. SHC1 knockdown altered 2,344 proteins, including 972 upregulated and 1,372 downregulated proteins, distributed mainly in the nucleus, cytoplasm, extracellular space, plasma membrane, and mitochondria (Fig. S6C, D). Integrated transcriptomic and proteomic analysis highlighted CCNB1 as the most significantly altered cell-cycle regulator, followed by CDC20 (Fig. S6E). RNA-seq and Western blot (WB) validation confirmed substantial CCNB1 downregulation (Fig. 5D).

Given the profound impact of SHC1 downregulation on DNA replication and repair pathways, we next assessed whether SHC1 depletion affects sensitivity to TMZ—a DNA-alkylating agent that induces O^6-methylguanine adducts and lethal double-strand breaks via aberrant mismatch repair [28]. As expected, TMZ treatment caused a greater reduction in cell viability and accelerated cell death in SHC1-knockdown cells than in control U251MG and GL261 cells across a range of concentrations (Fig. 5E). This chemosensitizing effect was further validated in U251MG and LN229 cells by CCK-8 assays following combined TMZ and SHC1 knockdown treatment (Fig. 5F). Taken together, these results link SHC1-mediated cell-cycle and DNA-repair regulation to chemoresistance and support SHC1 as a candidate target for TMZ combination therapy.

SHC1 knockdown suppresses GBM progression through CCNB1 downregulation

CCNB1 is a core mitotic cyclin that binds CDK1 to form the maturation-promoting factor and functions as a molecular switch controlling passage through the G_2/M checkpoint. Given that SHC1 knockdown induced pronounced G_2/M arrest and

substantially reduced CCNB1 at both the transcript and protein levels, we hypothesized that CCNB1 mediates SHC1-dependent cell-cycle progression. To validate this causal relationship, CCNB1 rescue experiments were conducted in SHC1-knockdown U251MG and LN229 cells (Fig. S7A, B). Exogenous CCNB1 significantly reduced the proportion of cells accumulated in G_2/M relative to SHC1 knockdown alone (Fig. 6A), demonstrating partial restoration of cell-cycle progression. Functionally, CCNB1 re-expression restored overall proliferative capacity and increased the proportion of proliferating GBM cells (Fig. 6B, C, S7C). It also partially rescued migration and invasion (Fig. 6D, S7D, E) and attenuated the apoptosis induced by SHC1 depletion (Fig. 6E). Colony-formation assays further confirmed that CCNB1 overexpression counteracted the suppressive effect of SHC1 knockdown on long-term proliferative capacity (Fig. 6F). Overall these findings identify CCNB1 downregulation as a key molecular event linking SHC1 loss to G_2/M arrest, proliferation inhibition, impaired migration and invasion, and apoptosis, thereby supporting CCNB1 as a major downstream effector through which SHC1 maintains the malignant phenotype of GBM cells.

Downregulation of SHC1 significantly suppresses GBM tissue in vivo and remodels the tumor immune microenvironment

To validate the SHC1–CCNB1 axis and determine whether SHC1 loss sensitizes GBM to TMZ in vivo, an intracranial U251MG-Luc nude-mouse model was established. Mice were assigned to control, shSHC1, shSHC1 + CCNB1, TMZ, or shSHC1 + TMZ groups. TMZ was administered via intraperitoneal injection at 50 mg/kg once daily for

five consecutive days, and bioluminescence imaging of intracranial tumors was performed on day 18 post-implantation to assess tumor burden (Fig. 7A, B, S8A, B). Compared with the shSHC1 group, restoration of CCNB1 significantly increased intracranial tumor signals, indicating that CCNB1 overexpression partially reversed the growth suppression caused by SHC1 deficiency. As expected, TMZ monotherapy failed to effectively suppress tumor signals in control mice, whereas TMZ treatment in SHC1-knockdown tumors markedly reduced bioluminescence, indicating that SHC1 deficiency increases GBM sensitivity to TMZ in vivo.

Survival analysis further supported these findings. SHC1 knockdown significantly prolonged overall survival compared with the control group. Conversely, CCNB1 restoration largely abrogated the survival benefit conferred by SHC1 knockdown, resulting in a survival profile comparable to that of control mice and supporting CCNB1 as a primary downstream mediator of the in vivo pro-tumorigenic effects of SHC1 (Fig. 7C). TMZ alone did not significantly prolong survival, while the combination of SHC1 knockdown and TMZ produced a further significant survival benefit (Fig. S8C). Histological analysis yielded findings consistent with the imaging and survival data: hematoxylin and eosin (H&E) and Ki-67 staining showed marked tumor shrinkage and a reduced proportion of Ki-67-positive cells after SHC1 knockdown, whereas tumor tissue was virtually absent in the shSHC1 + TMZ group (Fig. 7D, E, S8D). Collectively, these data demonstrate that SHC1 promotes GBM growth through CCNB1 and that SHC1 depletion substantially enhances TMZ responsiveness in vivo.

Finally, given that SHC1 expression correlated with immunosuppressive cell

infiltration and inflammatory/interferon response pathways in human GBM, we evaluated its immune effects using GL261 allografts in immunocompetent C57BL/6 mice. Shc1 knockdown significantly reduced intracranial tumor burden, prolonged overall survival, and decreased the abundance of Ki-67-positive tumor cells (Fig. 7F–I, S8E). Immunofluorescence staining further revealed a significant increase in the proportion of $CD8^+$ T cells within shShc1 GBM tissues compared with controls (Fig. 7J). To characterize the immune microenvironment at single-cell resolution, we performed scRNA-seq on intracranial GBM tissues and annotated the major cell populations (Fig. 7K). While the overall proportions of immune cell subsets were largely comparable between the two groups (Fig. 7L), we observed a marked increase in the absolute number of $CD8^+$ T cells in the shShc1 group relative to controls (1,982 vs. 1,109; Fig. 7M). These results collectively indicate that SHC1 knockdown suppresses GBM growth in immunocompetent hosts and is associated with enhanced $CD8^+$ T cell infiltration within the tumor microenvironment. Thus, SHC1 may function as both a tumor-intrinsic driver and an immune-microenvironment regulator, positioning it as a promising candidate for GBM therapy and for sensitizing tumors to TMZ.

Discussion

Over the years, research has shown that SHC1 encodes three isoforms with distinct functions [29]. p46Shc predominantly resides in the mitochondrial matrix, where it interacts with and suppresses mitochondrial 3-ketoacyl-CoA thiolase ACAA2, contributing to the regulation of fatty acid β-oxidation and cellular energy metabolism

[30,31]. Besides, p52Shc is recruited to the cell membrane upon receptor tyrosine kinase activation and, through complex formation with signaling molecules such as GRB2, transmits upstream receptor signals, including those from EGFR, to the RAS–RAF–MEK–ERK axis, thereby regulating cell proliferation, survival, and differentiation [32–35]. Besides, p66Shc, the largest isoform, uniquely contains a CH2 domain critical for mitochondrial ROS production and apoptosis [36,37]. It is now understood that under stress conditions, p66Shc can function within mitochondria; its cytochrome c-binding region facilitates electron transfer with mitochondrial cytochrome c, promoting ROS generation and thereby regulating oxidative stress, mitochondrial homeostasis, and apoptosis [38–41]. Beyond growth factor-induced proliferation, p66Shc has been implicated in cell migration and adhesion [42,43]. In GBM, SHC1 downregulation has been reported to inhibit U87MG cell proliferation [23]; however, the mechanisms linking SHC1 to GBM progression remain insufficiently explored.

Herein, we initially conducted pan-cancer analysis and observed significantly increased SHC1 expression across multiple tumor types relative to peritumoral tissues. Interestingly, when GBM patients were stratified by SHC1 expression at the optimal cutoff, a significant survival difference emerged, whereas stratification by the median expression level did not yield a significant difference. More importantly, SHC1 appeared more closely associated with GBM recurrence and chemoresistance, as significant differences emerged when patients were stratified by the median value. Transcriptomic profiling further showed that SHC1 knockdown markedly suppressed

multiple DNA repair pathways. Given that TMZ, the first-line chemotherapeutic agent for GBM, exerts cytotoxicity through O^6-methylguanine adduct formation and subsequent mismatch repair-dependent DNA double-strand breaks [28,44], our finding that SHC1 knockdown enhances TMZ sensitivity suggests that SHC1 may contribute to the regulation of DNA damage responses and chemoresistance in GBM. However, the mechanisms driving this sensitization remain to be fully elucidated.

Analysis of single-cell transcriptomic data revealed that SHC1 expression is largely restricted to malignant cells. ssGSEA further revealed that GBM patients with elevated SHC1 expression exhibited significantly higher immune scores and greater immune cell infiltration, with the mesenchymal subtype demonstrating the highest degree of immune infiltration, a pattern that may arise from a bidirectional interplay between malignant cells and the surrounding immune milieu [25,45]. Consistently, SHC1 expression in GBM tissues showed positive associations with $CD4^+$ T cells, macrophage infiltration, and neutrophils, indicating a potential role for SHC1 in regulating tumor progression via the immune microenvironment.

Although p66Shc has been associated with prostate cancer proliferation and cell cycle modulation [46], its role in GBM has remained unclear. Our study demonstrated that SHC1 silencing in GBM cells markedly reduced proliferative and migratory capacities, enhanced apoptosis, and triggered cell cycle arrest. In an orthotopic GBM model using immunodeficient NCG mice, SHC1 knockdown significantly restricted tumor progression, confirming that SHC1 can directly promote GBM cell proliferation independently of immune system involvement. Mechanistically, both transcriptomic

and proteomic analyses converged on cell cycle pathways as the most significantly altered, with CCNB1 emerging as a key downregulated molecule. CCNB1, a mitotic cyclin essential for the G_2/M transition [47,48], mediated SHC1's effects on cell cycle progression, as CCNB1 overexpression partially rescued the proliferation, migration, and apoptosis phenotypes induced by SHC1 knockdown. Moreover, SHC1 knockdown compromised DNA repair capacity and sensitized GBM cells to TMZ, effects that were consistently observed in vivo. In nude mouse models, SHC1 knockdown suppressed intracranial tumor growth, an effect that was largely reversed by CCNB1 overexpression. Besides, SHC1 downregulation significantly enhanced TMZ efficacy. In immunocompetent C57BL/6 mice, SHC1 knockdown further promoted $CD8^+$ T cell infiltration and macrophage repolarization toward the M1 phenotype, suggesting that SHC1 contributes to the regulation of the tumor immune microenvironment.

Nevertheless, several limitations of this study should be acknowledged. The molecular basis underlying SHC1-mediated regulation of CCNB1 expression and DNA repair pathways remains incompletely understood. Moreover, the lack of clinical sample validation limits the direct translational relevance of our observations. Nevertheless, the consistent convergence of multi-omics and functional data provides a robust foundation for our conclusions and offers clear directions for future investigations.

In summary, SHC1 is significantly overexpressed in multiple tumor types and serves as a prognostic risk factor in several malignancies. Within GBM, SHC1 is mainly detected in malignant cells, and its expression level correlates positively with the

accumulation of immunosuppressive cell types, namely M2-polarized macrophages, regulatory T cells, and neutrophils, suggesting a role for SHC1 in driving immune evasion through microenvironmental remodeling. Functional in vitro and in vivo experiments confirmed that SHC1 knockdown substantially inhibits malignant progression in GBM. Mechanistically, SHC1 drives GBM proliferation and survival primarily by modulating cell cycle progression and DNA damage repair pathways. Collectively, this study reveals a dual oncogenic role for SHC1 in GBM, promoting tumor-intrinsic proliferation and repair while concurrently shaping an immunosuppressive microenvironment, providing a strong rationale for targeting SHC1 as a therapeutic strategy and offering a candidate approach for GBM treatment.

MATERIALS AND METHODS

Data sourcing and preprocessing

In the present study, multiple bioinformatics resources were used to systematically investigate the expression and genomic characteristics of SHC1. Multi-omics data and clinical annotations across human cancers were obtained from UCSC Xena (https://xena.ucsc.edu/) [49], which provides preprocessed and batch-adjusted datasets from GTEx (https://gtexportal.org/home/datasets) and TCGA (https://portal.gdc.cancer.gov). SHC1 protein expression was evaluated using UALCAN (http://ualcan.path.uab.edu/analysis.html) based on CPTAC data, and GEPIA3 (https://gepia3.bioinfoliu.com) was employed to analyze SHC1 expression in GBM. Genomic alteration profiles, including mutation frequencies and variant

classifications, were assessed via cBioPortal (https://www.cbioportal.org/). HPA (https://www.proteinatlas.org) was used to determine the subcellular localization of SHC1. A high-confidence PPI network (score ≥ 0.95) was also constructed via STRING (https://cn.string-db.org/) to screen for potential SHC1-interacting partners.

Cross-cancer prognostic analysis of SHC1

Transcriptomic and clinical data for 33 cancer types were acquired from TCGA via UCSC Xena to evaluate the prognostic value of SHC1. Survival was evaluated using OS, PFI, DSS, and DFI endpoints. The relationship between SHC1 expression and patient outcomes was examined using univariate Cox regression and Kaplan–Meier analyses, performed in R with the "survival" package to obtain log-rank P values, HRs, and 95% CIs. Results were presented as a heatmap, with OS findings further detailed in a forest plot generated using "forestplot".

GSEA for SHC1

For each TCGA cancer type, samples were stratified into SHC1-high and SHC1-low groups based on median expression. Samples were divided into SHC1-high and SHC1-low subgroups according to median SHC1 expression. Differentially expressed genes (DEGs) between the two subgroups were analyzed by GSEA against the Hallmark gene sets (h.all.v7.4.symbols.gmt) from MSigDB, with genes ranked by logFC. NES and FDR values were calculated using the R "clusterProfiler" package, and the resulting enrichment data were visualized as bubble plots via "ggplot2".

Tumor immunity and immune infiltration analysis

TIMER2.0 (https://compbio.cn/timer/2) was used to assess immune infiltration patterns.

Spearman's rank correlation was applied to examine the relationship between SHC1 expression and the infiltration levels of 21 immune cell types across multiple cancers, covering adaptive immune cells ($CD4^+$ T, $CD8^+$ T, Tregs, B cells, γδT, and NKT), innate immune cells (macrophages, NK cells, neutrophils, monocytes, mast cells, eosinophils, and dendritic cells), as well as MDSCs, progenitor/precursor cells, and stromal elements (cancer-associated endothelial cells and fibroblasts).

Single-cell RNA sequencing analysis

SHC1 expression at the single-cell level was examined via the TISCH2 database (https://tisch.compbio.cn/) [50]. SHC1 expression was examined across 78 cancer lineages and 33 cell types at the "major-lineage" annotation level.

ssGSEA in GBM

ssGSEA was used to quantify immune cell infiltration from RNA-seq transcriptomic profiles. 29 immune cell types and their functional features were assessed in TCGA glioma specimens. Samples were dichotomized into high- and low-SHC1 expression subgroups based on the median expression value. Tumor purity, immune, and stromal scores for each glioma sample were calculated using the "ESTIMATE" algorithm in R.

Materials and antibodies

Antibodies against SHC1 (12496-1-AP), GAPDH (60004-1-Ig), CDC20 (10252-1-AP), CCNB1 (55004-1-AP), and Ki-67 (27309-1-AP) were purchased from Proteintech (China). Dimethyl sulfoxide (DMSO, D8371) was obtained from Solarbio (China). Puromycin (KE2972) and temozolomide (TMZ, KM11811) were purchased from KKLmed.INC (USA). D-Luciferin potassium salt (SB-D1007) was procured from

Share Bio (China).

Cell culture

HEK 293T (GNHu44), LN229 (SCSP-5352), and U251MG (TChu-58) cell lines were obtained from the Cell Bank of the Chinese Academy of Sciences (https://www.cellbank.org.cn/), while murine GL261 cells were purchased from iCell Bioscience Inc. (China, iCell-m063). All cells were maintained in Dulbecco's Modified Eagle Medium (DMEM, Gibco, 11995065) supplemented with 10% fetal bovine serum (FBS, Azaood, AD00006) at 37 °C in a 5% CO_2 humidified incubator.

Plasmid construction and lentivirus packaging

Lentiviral-mediated SHC1 knockdown was achieved using the pLVX-shRNA2 vector carrying shRNA sequences targeting human SHC1 or mouse Shc1, with a non-targeting shRNA as the negative control (sequences provided in Table S1). For CCNB1 overexpression, its coding sequence was PCR-amplified from U251MG cDNA and subcloned into pcDNA3.1(+). All recombinant plasmids were prepared using the ClonExpress II One-Step Cloning Kit (Vazyme, C112) as per the manufacturer's recommendations.

Lentiviral particles were generated by co-transfecting HEK 293T cells (~80% confluent) with the shRNA-expressing construct and the helper plasmids pMD2.G and psPAX2 via Lipofectamine 3000 (Invitrogen, L3000015). Lentiviral supernatants were harvested on days 2 and 3 after transfection, combined, and concentrated with a lentivirus concentration kit (V2001, BIOMIGA). The concentrated virus was filtered through a 0.22-μm syringe membrane. Target cells were transduced with the filtered

virus in medium supplemented with 8 μg/mL polybrene. After 24 h of incubation, the virus-containing medium was replaced with fresh complete growth medium supplemented with 2 μg/mL puromycin. Cells were cultured under continuous selection for 5 days to establish stably transduced populations

WB and real-time quantitative PCR (RT-qPCR)

Cells were washed with PBS and lysed in RIPA buffer (Solarbio, R0020) on ice for 15-30 min. After centrifugation at 12,000 rpm for 10 min at 4 °C, the supernatants were collected. Protein samples were mixed with 5× loading buffer (Solarbio, P1040), denatured at 100 °C for 8 min, and resolved by 10% or 12% SDS-PAGE (25 μg protein per lane), followed by transfer onto PVDF membranes. The membranes were blocked with 5% BSA (Solarbio, A8010) and incubated with primary antibodies at 4 °C overnight. After three 10-min TBST washes, the blots were probed with HRP-conjugated secondary antibodies for 1–2 h at room temperature. Immunoreactive signals were visualized using ECL substrate and captured with a chemiluminescence imaging system (Tanon, China). Band intensities were quantified with ImageJ (version 1.53t).

Cell Proliferation Assay (CCK-8)

Cell viability was evaluated using the CCK-8 assay (Solarbio, CA1210). Briefly, GBM cells were seeded into 96-well plates at 2×10^3 cells/well and cultured for up to 5 days. At each 24-h interval, 10 μL of CCK-8 reagent was added, followed by 30-min incubation at 37 °C, and the optical density was recorded at 450 nm using a microplate reader.

Colony Formation Assay

GBM cells in logarithmic growth were plated into 6-well plates (500 cells/well) and incubated at 37 °C in 5% CO_2 for 14 days. The resulting colonies were then fixed in 4% PFA (Biosharp, BL539A) for 30 min at ambient temperature, stained with 0.5% crystal violet (Solarbio, G1062), and counted manually after rinsing.

Wound healing assay

Confluent GBM monolayers in 6-well plates were scratched with a sterile 100-μL pipette tip. Debris was removed by washing twice with pre-warmed PBS, and fresh medium was subsequently added. Images of the scratched areas were captured at 0 and 48 h, and migration was evaluated by measuring the wound-closure rate.

EdU incorporation assay

EdU incorporation (Beyotime, C0078L) was used to assess cell proliferation. GBM cells seeded in 6-well plates were incubated with 10 μM EdU for 1-2 h at 37 °C. After fixation and permeabilization, nuclei were counterstained with Hoechst 33342 (Solarbio, C0031). EdU-positive cells were visualized under a fluorescence microscope, and the percentage of EdU-positive nuclei was calculated using ImageJ (version 1.54g).

Transwell invasion assay

Invasion was evaluated using 24-well Transwell inserts (8-μm pore size) pre-coated with Matrigel (Corning, 354234) at 37 °C for 4 h. GBM cells resuspended in serum-free DMEM were added to the upper compartment at 5×10^4 cells/well, while the lower chamber received complete medium with 10% FBS as a chemoattractant. After 24 h of incubation at 37 °C, non-invading cells on the upper membrane surface were removed

with a cotton swab. Invaded cells on the lower surface of the membrane were fixed with 4% PFA, stained with 0.1% crystal violet (Solarbio, G1063), and imaged in random fields for cell counting. Cell counts were determined using ImageJ.

Cell cycle and apoptosis analysis

For cell-cycle analysis, cells were plated in 6-well plates and transfected with shRNA or control plasmids. At 48 h post-transfection, cells were collected, washed twice with PBS, and fixed overnight in 75% ethanol at 4 °C. Fixed cells underwent 0.5 h staining with propidium iodide (PI) at room temperature before DNA content was quantified on a CytoFLEX flow cytometer (B3 R3 V2; Beckman Coulter). Cell cycle distribution was quantified with ModFit 5.0 software.

To evaluate apoptosis, both floating and adherent cells were collected, resuspended in 100 μL of binding buffer, and stained with 5 μL PI and 4-5 μL Annexin V-FITC for 10-15 min on ice in the dark. After staining, the volume was adjusted to 500 μL with binding buffer prior to flow cytometric analysis.

RNA Sequencing Analysis

Stable SHC1-silenced U251MG and GL261 cells, together with corresponding controls, were harvested for RNA sequencing. Total RNA was extracted with RNAiso Plus reagent (Takara, #9109) following the manufacturer's instructions, and high-throughput sequencing was performed by Tsingke Biotechnology. Raw sequencing reads were quality-filtered and trimmed using fastp (v0.23.4) to remove adapter sequences and low-quality bases ($Q < 20$). Using GRCh38 as the human reference genome, filtered reads were aligned, gene-level counts were generated by FeatureCounts, and expression

was normalized to RPKM.

Proteomics analysis

Cells were harvested at the specified times, washed with cold PBS, and subsequently lysed in protease-inhibitor-supplemented buffer. After sonication and high-speed centrifugation, supernatants were collected for BCA-based protein quantification. Equal quantities of protein underwent sequential reduction, alkylation, and trypsin digestion. Peptides were subsequently desalted, purified, and analyzed by nano-LC coupled to high-resolution tandem mass spectrometry.

Animal experiments

All animal experiments were approved by the Institutional Animal Care and Use Committee of Nanchang University (Approval No. NCULAE-20260627001) and conducted in accordance with relevant ethical guidelines. Five-week-old male BALB/c nude mice (GemPharmatech, China) were used for intracranial xenografting. SHC1-silenced U251MG-Luc cells and control cells were suspended in ice-cold PBS, and 1.5 $\times 10^5$ cells in 6 μL PBS were stereotactically injected into the right frontal lobe of isoflurane-anesthetized mice. The needle was left in place for 5 min, then slowly withdrawn, and the skull opening was sealed with bone wax. Tumor growth was monitored via bioluminescence imaging using the IVIS Lumina Series III system (PerkinElmer). Mice were euthanized when distress or seizures developed. For histological evaluation, harvested brains were fixed in 4% PFA.

Histological and IHC Staining

Following 4% PFA fixation, mouse brains were paraffin-embedded and sectioned at 3

μm. After dewaxing and rehydration, sections were stained with H&E for histopathological examination, then dehydrated, cleared, and coverslipped. For IHC, sections underwent antigen retrieval in citrate buffer (pH 6.0), endogenous peroxidase blocking, and overnight incubation with the primary antibody at 4 °C. This was followed by HRP-conjugated secondary antibody, DAB chromogenic reaction, and hematoxylin counterstaining. Images were captured under a light microscope, and H-scores were calculated with Servicebio analysis software (China).

Single-Cell RNA Sequencing of Mouse GBM Tissues

For single-cell transcriptomic profiling, mouse GBM tissues were dissected and immediately placed in tissue preservation solution at 4 °C. Tissues were minced and dissociated into single-cell suspensions. After quality control, library preparation and sequencing were performed by Tsingke Biotechnology Co., Ltd. Processing and analysis of raw sequencing data followed standard single-cell bioinformatics workflows.

Statistical Analysis

Statistical analyses were performed using R (version 4.2.0) and GraphPad Prism 9.0. All data were expressed as mean ± standard deviation (SD) from at least three independent replicates. Group comparisons were conducted using two-tailed Student's t-test for two groups and two-way ANOVA for multiple groups. Pearson correlation analysis and Kaplan–Meier survival analysis with log-rank tests were applied where appropriate. Statistical significance was defined as $P < 0.05$, with significance levels indicated as follows: ns, not significant; *$P < 0.05$; **$P < 0.01$; ***$P < 0.001$; ****P

< 0.0001.

DATA AVAILABILITY

All data supporting the findings of this study are available within the paper and its Supplementary Information. The RNA-seq data have been deposited in the NCBI Sequence Read Archive (SRA) under accession number PRJNA1529908 and PRJNA1533612. The proteomics data are available in Supplementary Table S2. All other data are available from the corresponding author upon reasonable request.

References

1. Chen S, Cao Z, Prettner K, Kuhn M, Yang J, Jiao L, Wang Z, Li W, Geldsetzer P, Bärnighausen T, et al. Estimates and Projections of the Global Economic Cost of 29 Cancers in 204 Countries and Territories From 2020 to 2050. *JAMA Oncol* (2023) **9**:465. doi:10.1001/jamaoncol.2022.7826

2. Bray F, Laversanne M, Sung H, Ferlay J, Siegel RL, Soerjomataram I, Jemal A. Global cancer statistics 2022: GLOBOCAN estimates of incidence and mortality worldwide for 36 cancers in 185 countries. *CA A Cancer J Clinicians* (2024) **74**:229–263. doi:10.3322/caac.21834

3. Zhang Y, Zhang Z. The history and advances in cancer immunotherapy: understanding the characteristics of tumor-infiltrating immune cells and their therapeutic implications. *Cell Mol Immunol* (2020) **17**:807–821. doi:10.1038/s41423-020-0488-6

4. Weller M, Van Den Bent M, Preusser M, Le Rhun E, Tonn JC, Minniti G, Bendszus M, Balana C, Chinot O, Dirven L, et al. EANO guidelines on the diagnosis and treatment of diffuse gliomas of adulthood. *Nat Rev Clin Oncol* (2021) **18**:170–186. doi:10.1038/s41571-020-00447-z

5. Mir HA, Ali R, Mushtaq U, Khanday FA. Structure-functional implications of longevity protein p66Shc in health and disease. *Ageing Research Reviews* (2020) **63**:101139. doi:10.1016/j.arr.2020.101139

6. Zaeifi D, Jamialahmadi K, Karimi G. The Role of P66SHC in Cancer: Molecular Mechanisms and Therapeutic Implications. *J Cellular Molecular Medi* (2025) **29**:e70737. doi:10.1111/jcmm.70737

7. Jiang T, Qin T, Gao P, Tao Z, Wang X, Wu M, Gu J, Chu B, Zheng Z, Yi J, et al. SIRT1 attenuates blood-spinal cord barrier disruption after spinal cord injury by deacetylating p66Shc. *Redox Biology* (2023) **60**:102615. doi:10.1016/j.redox.2023.102615

8. Li Y, Dong Y, He Y, Zheng J, Liu H, Li L, Hao X, Zhao Y, Yang Z, Sun Y, et al. Endothelial Cell-Based Vascular Bandages for Blood–Brain Barrier Repair and Targeted siRNA Delivery. *Advanced Science* (2026) **13**:e17780. doi:10.1002/advs.202517780

9. Potes Y, Bermejo-Millo JC, Mendes C, Castelão-Baptista JP, Díaz-Luis A, Pérez-Martínez Z, Solano JJ, Sardão VA, Oliveira PJ, Caballero B, et al. p66Shc signaling and autophagy impact on C2C12 myoblast differentiation during senescence. *Cell Death Dis* (2024) **15**:200. doi:10.1038/s41419-024-06582-0

10. Powell AM, Cumming RC, Betts DH. p66Shc deletion confers apoptotic resistance to loss of EGFR-ERK signalling in neural stem cells. *Cell Death Dis* (2025) **16**:479. doi:10.1038/s41419-025-07778-8

11. Gierhardt M, Pak O, Sydykov A, Kraut S, Schäffer J, Garcia C, Veith C, Zeidan EM, Brosien M, Quanz K, et al. Genetic deletion of p66shc and/or cyclophilin D results in decreased pulmonary vascular tone. *Cardiovascular Research* (2022) **118**:305–315. doi:10.1093/cvr/cvaa310

12. Yeh Y-T, Lee C-I, Lim SH, Chen L-J, Wang W-L, Chuang Y-J, Chiu J-J. Convergence of physical and chemical signaling in the modulation of vascular smooth muscle cell cycle and proliferation by fibrillar collagen-regulated P66Shc. *Biomaterials* (2012) **33**:6728–6738. doi:10.1016/j.biomaterials.2012.06.030

13. Jiang X, Edstrom E, Altun M, Ulfhake B. Differential regulation of Shc adaptor proteins in skeletal muscle, spinal cord and forebrain of aged rats with sensorimotor impairment. *Aging Cell* (2003) **2**:47–57. doi:10.1046/j.1474-9728.2003.00030.x

14. Zhang W, Liu W, Zhong X, Dai L, Liu X, Li S, Jiang H, He X, Dong W, Lu L, et al. Epigenetic and O-glycosylation regulation of p66Shc mitigates mitochondrial oxidative stress in aortic dissection. *Theranostics* (2026) **16**:4394–4410. doi:10.7150/thno.124508

15. Haines E, Saucier C, Claing A. The Adaptor Proteins p66Shc and Grb2 Regulate the Activation of the GTPases ARF1 and ARF6 in Invasive Breast Cancer Cells. *Journal of Biological Chemistry* (2014) **289**:5687–5703. doi:10.1074/jbc.M113.516047

16. Lewis K, Kiepas A, Hudson J, Senecal J, Ha JR, Voorand E, Annis MG, Sabourin V, Ahn R, La Selva R, et al. p66ShcA functions as a contextual promoter of breast cancer metastasis. *Breast Cancer Res* (2020) **22**:7. doi:10.1186/s13058-020-1245-6

17. Rajendran M, Thomes P, Zhang L, Veeramani S, Lin M-F. p66Shc—a longevity redox protein in human prostate cancer progression and metastasis: p66Shc in cancer progression and metastasis. *Cancer Metastasis Rev* (2010) **29**:207–222. doi:10.1007/s10555-010-9213-8

18. Xiao D, Singh SV. p66Shc Is Indispensable for Phenethyl Isothiocyanate–Induced Apoptosis in Human Prostate Cancer Cells. *Cancer Research* (2010) **70**:3150–3158. doi:10.1158/0008-5472.CAN-09-4451

19. Grossman SR, Lyle S, Resnick MB, Sabo E, Lis RT, Rosinha E, Liu Q, Hsieh C-C, Bhat G, Frackelton AR, et al. p66 Shc Tumor Levels Show a Strong Prognostic Correlation with Disease Outcome in Stage IIA Colon Cancer. *Clinical Cancer Research* (2007) **13**:5798–5804. doi:10.1158/1078-0432.CCR-07-0073

20. Liu G, Xie B, Gong L, Zhou J, Shu G. The Expression of p66Shc Protein in Benign, Premalignant, and Malignant Gastrointestinal Lesions. *Pathol Oncol Res* (2014) **20**:733–739. doi:10.1007/s12253-014-9754-1

21. Huang P, Feng X, Zhao Z, Yang B, Fang T, Guo M, Xia J. p66Shc promotes HCC progression in the tumor microenvironment via STAT3 signaling. *Experimental Cell Research* (2019) **383**:111550. doi:10.1016/j.yexcr.2019.111550

22. Liu Y, Zhang X, Yang B, Zhuang H, Guo H, Wei W, Li Y, Chen R, Li Y, Zhang N. Demethylation-Induced Overexpression of Shc3 Drives c-Raf–Independent Activation of MEK/ERK in HCC. *Cancer Research* (2018) **78**:2219–2232. doi:10.1158/0008-5472.CAN-17-2432

23. Peng G, Feng Y, Wang X, Huang W, Li Y. The mitochondria-related gene risk mode revealed p66Shc as a prognostic mitochondria-related gene of glioblastoma. *Sci Rep* (2024) **14**:11418. doi:10.1038/s41598-024-62083-2

24. Mir HA, Ali R, Mushtaq U, Khanday FA. Structure-functional implications of longevity protein p66Shc in health and disease. *Ageing Research Reviews* (2020) **63**:101139. doi:10.1016/j.arr.2020.101139

25. Hara T, Chanoch-Myers R, Mathewson ND, Myskiw C, Atta L, Bussema L, Eichhorn SW, Greenwald AC, Kinker GS, Rodman C, et al. Interactions between cancer cells and immune cells drive transitions to mesenchymal-like states in glioblastoma. *Cancer Cell* (2021) **39**:779-792.e11. doi:10.1016/j.ccell.2021.05.002

26. Liu Y, Zhou F, Ali H, Lathia JD, Chen P. Immunotherapy for glioblastoma: current state, challenges, and future perspectives. *Cell Mol Immunol* (2024) **21**:1354–1375. doi:10.1038/s41423-024-01226-x

27. Moreno-Sanchez PM. Immunosuppressive mechanisms and therapeutic interventions shaping glioblastoma immunity.

28. Roos WP, Batista LFZ, Naumann SC, Wick W, Weller M, Menck CFM, Kaina B. Apoptosis in malignant glioma cells triggered by the temozolomide-induced DNA lesion O6-methylguanine. *Oncogene* (2007) **26**:186–197. doi:10.1038/sj.onc.1209785

29. Pellegrini M, Pacini S, Baldari CT. p66SHC: The apoptotic side of Shc proteins. *Apoptosis* (2005) **10**:13–18. doi:10.1007/s10495-005-6057-8

30. Li Y, Jiang JX, Fan W, Fish SR, Das S, Gupta P, Mozes G, Vancza L, Sarkar S, Kunimoto K, et al. Shc Is Implicated in Calreticulin-Mediated Sterile Inflammation in Alcoholic Hepatitis.

Cellular and Molecular Gastroenterology and Hepatology (2023) **15**:197–211. doi:10.1016/j.jcmgh.2022.09.005

31. Li Y, Fan W, Lo T-H, Jiang JX, Fish SR, Tomilov A, Chronopoulos A, Bansal V, Mozes G, Vancza L, et al. P46Shc Inhibits Mitochondrial ACAA2 Thiolase, Exacerbating Mitochondrial Injury and Inflammation in Aging Livers. *The American Journal of Pathology* (2025) **195**:528–541. doi:10.1016/j.ajpath.2024.10.022

32. Lebiedzinska-Arciszewska M, Pakula B, Bonora M, Missiroli S, Potes Y, Jakubek-Olszewska P, Simoes ICM, Pinton P, Wieckowski MR. Distribution of the p66Shc Adaptor Protein Among Mitochondrial and Mitochondria—Associated Membranes Fractions in Normal and Oxidative Stress Conditions. *IJMS* (2024) **25**:12835. doi:10.3390/ijms252312835

33. Ingersoll MA, Chou Y-W, Lin JS, Yuan T-C, Miller DR, Xie Y, Tu Y, Oberley-Deegan RE, Batra SK, Lin M-F. p66Shc regulates migration of castration-resistant prostate cancer cells. *Cellular Signalling* (2018) **46**:1–14. doi:10.1016/j.cellsig.2018.02.008

34. Liang Y, Lei Y, Du M, Liang M, Liu Z, Li X, Gao Y. The increased expression and aberrant methylation of SHC1 in non–small cell lung cancer: Integrative analysis of clinical and bioinformatics databases. *J Cellular Molecular Medi* (2021) **25**:7039–7051. doi:10.1111/jcmm.16717

35. Furlan T, Khalid S, Nguyen A, Günther J, Troppmair J. The oxidoreductase p66Shc acts as tumor suppressor in BRAFV 600E-transformed cells. *Molecular Oncology* (2018) **12**:869–882. doi:10.1002/1878-0261.12199

36. Kleman AM, Brown JE, Zeiger SLH, Hettinger JC, Brooks JD, Holt B, Morrow JD, Musiek ES, Milne GL, McLaughlin B. $p66^{shc}$'s role as an essential mitophaghic molecule in controlling neuronal redox and energetic tone. *Autophagy* (2010) **6**:948–949. doi:10.4161/auto.6.7.13007

37. Di Lisa F, Kaludercic N, Carpi A, Menabò R, Giorgio M. Mitochondrial pathways for ROS formation and myocardial injury: the relevance of p66Shc and monoamine oxidase. *Basic Res Cardiol* (2009) **104**:131–139. doi:10.1007/s00395-009-0008-4

38. Patrussi L, Giommoni N, Pellegrini M, Gamberucci A, Baldari CT. p66Shc-dependent apoptosis requires Lck and CamKII activity. *Apoptosis* (2012) **17**:174–186. doi:10.1007/s10495-011-0663-4

39. Boengler K, Bornbaum J, Schlüter K-D, Schulz R. P66shc and its role in ischemic cardiovascular diseases. *Basic Res Cardiol* (2019) **114**:29. doi:10.1007/s00395-019-0738-x

40. Di Stefano V, Cencioni C, Zaccagnini G, Magenta A, Capogrossi MC, Martelli F. p66ShcA modulates oxidative stress and survival of endothelial progenitor cells in response to high glucose. *Cardiovascular Research* (2009) **82**:421–429. doi:10.1093/cvr/cvp082

41. Giorgio M, Migliaccio E, Orsini F, Paolucci D, Moroni M, Contursi C, Pelliccia G, Luzi L, Minucci S, Marcaccio M, et al. Electron Transfer between Cytochrome c and p66Shc Generates

Reactive Oxygen Species that Trigger Mitochondrial Apoptosis. *Cell* (2005) **122**:221–233. doi:10.1016/j.cell.2005.05.011

42. Li X, Gao D, Wang H, Li X, Yang J, Yan X, Liu Z, Ma Z. Negative feedback loop between p66Shc and ZEB1 regulates fibrotic EMT response in lung cancer cells. *Cell Death Dis* (2015) **6**:e1708–e1708. doi:10.1038/cddis.2015.74

43. Patrussi L, Ulivieri C, Lucherini OM, Paccani SR, Gamberucci A, Lanfrancone L, Pelicci PG, Baldari CT. p52Shc is required for CXCR4-dependent signaling and chemotaxis in T cells. *Blood* (2007) **110**:1730–1738. doi:10.1182/blood-2007-01-068411

44. Sarkaria JN, Kitange GJ, James CD, Plummer R, Calvert H, Weller M, Wick W. Mechanisms of Chemoresistance to Alkylating Agents in Malignant Glioma. *Clinical Cancer Research* (2008) **14**:2900–2908. doi:10.1158/1078-0432.CCR-07-1719

45. Kaffes I, Szulzewsky F, Chen Z, Herting CJ, Gabanic B, Velázquez Vega JE, Shelton J, Switchenko JM, Ross JL, McSwain LF, et al. Human Mesenchymal glioblastomas are characterized by an increased immune cell presence compared to Proneural and Classical tumors. *OncoImmunology* (2019) **8**:e1655360. doi:10.1080/2162402X.2019.1655360

46. Veeramani S, Igawa T, Yuan T-C, Lin F-F, Lee M-S, Lin JS, Johansson SL, Lin M-F. Expression of p66Shc protein correlates with proliferation of human prostate cancer cells. *Oncogene* (2005) **24**:7203–7212. doi:10.1038/sj.onc.1208852

47. Xie B, Wang S, Jiang N, Li JJ. Cyclin B1/CDK1-regulated mitochondrial bioenergetics in cell cycle progression and tumor resistance. *Cancer Letters* (2019) **443**:56–66. doi:10.1016/j.canlet.2018.11.019

48. Lu G, Yi J, Gubas A, Wang Y-T, Wu Y, Ren Y, Wu M, Shi Y, Ouyang C, Tan HWS, et al. Suppression of autophagy during mitosis via CUL4-RING ubiquitin ligases-mediated WIPI2 polyubiquitination and proteasomal degradation. *Autophagy* (2019) **15**:1917–1934. doi:10.1080/15548627.2019.1596484

49. Goldman MJ, Craft B, Hastie M, Repečka K, McDade F, Kamath A, Banerjee A, Luo Y, Rogers D, Brooks AN, et al. Visualizing and interpreting cancer genomics data via the Xena platform. (2020)

50. Sun D, Wang J, Han Y, Dong X, Ge J, Zheng R, Shi X, Wang B, Li Z, Ren P, et al. TISCH: a comprehensive web resource enabling interactive single-cell transcriptome visualization of tumor microenvironment. *Nucleic Acids Research* (2021) **49**:D1420–D1430. doi:10.1093/nar/gkaa1020

FUNDING

This work was supported by the National Natural Science Foundation of China (Grant No. 82472828) and the China Postdoctoral Science Foundation (Grant No. 2026M792257).

AUTHOR CONTRIBUTIONS

KJL and XGZ conceptualized and supervised the overall study, designed the experiments, revised the manuscript, and provided funding support. YX performed most experiments, collected and analyzed the data, and wrote the original draft. ML and JHZ assisted with the animal experiments and data collection. All authors reviewed and approved the final manuscript and agreed to its submission.

COMPETING INTERESTS

The authors declare no competing interests.

ETHICS APPROVAL AND CONSENT TO PARTICIPATE

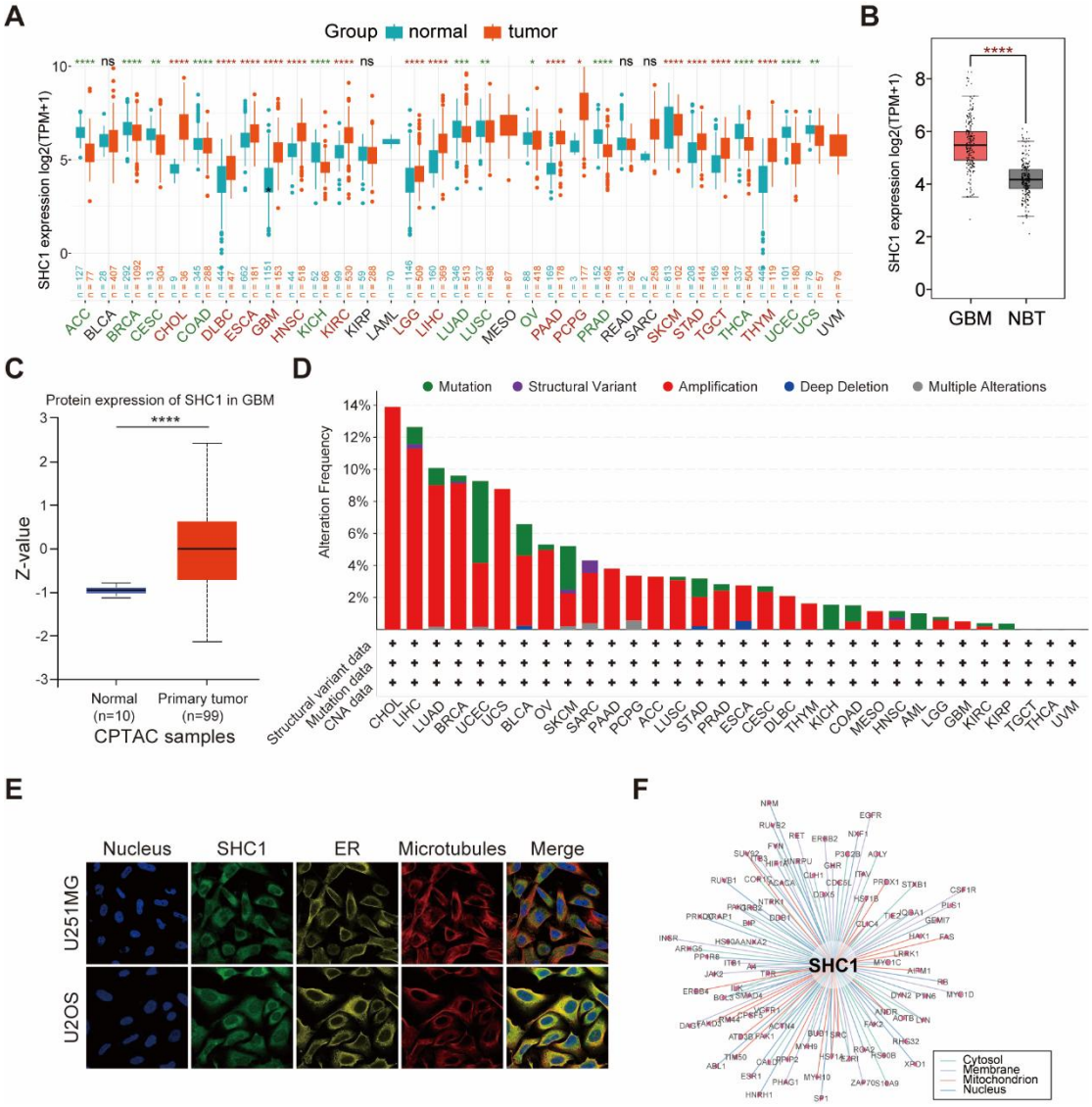
All animal experiments were approved by the Institutional Animal Care and Use Committee of Nanchang University (Approval No. NCULAE-20260627001). All procedures involving animals were performed in accordance with the ethical principles of laboratory animal welfare and were supervised by the committee and institutional laboratory managers.

CONSENT FOR PUBLICATION

All authors have read and approved the final manuscript and consented to its publication.

Figure Legends:

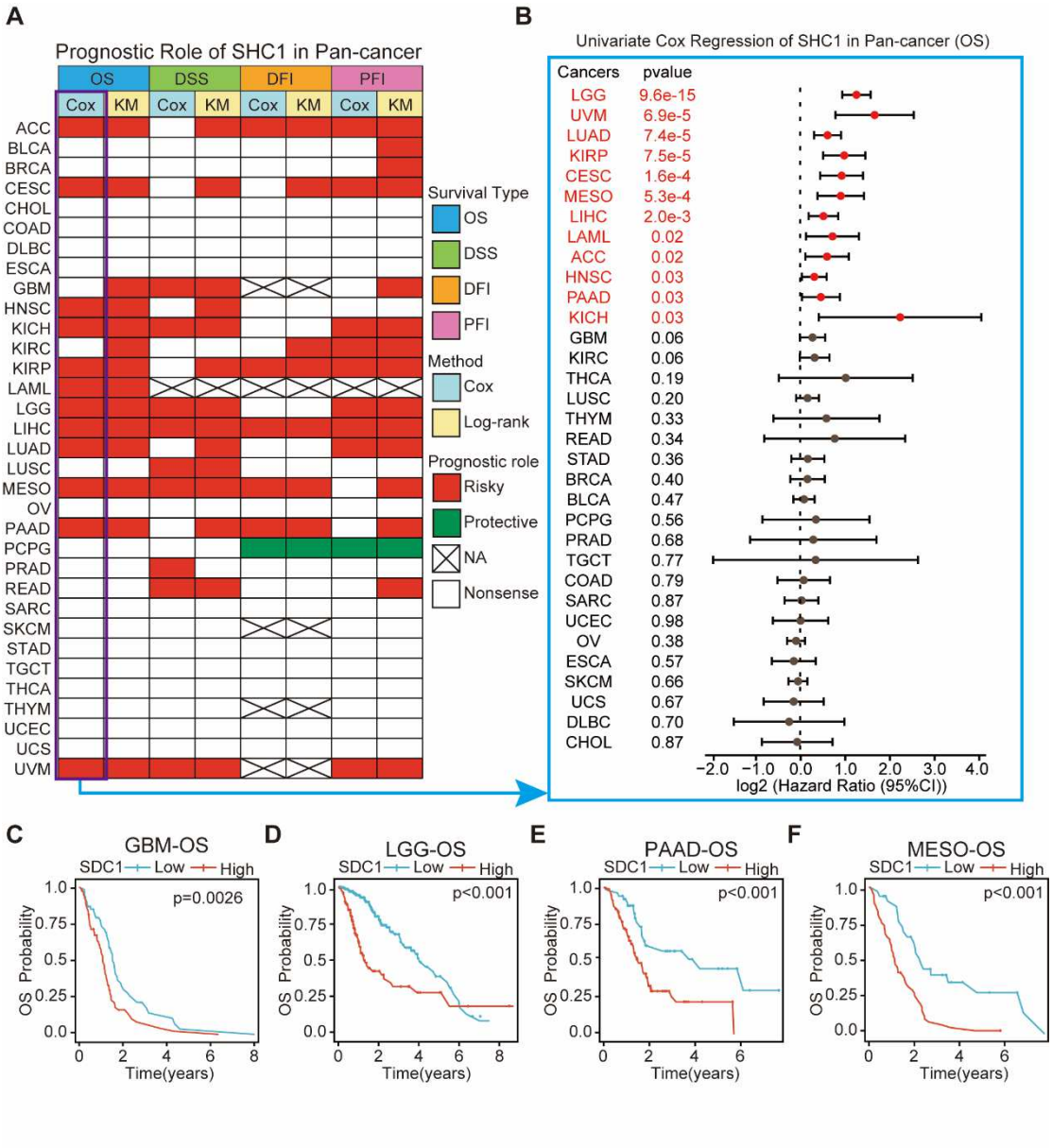
Figure 1. Expression landscape and genetic alterations of SHC1 in pan-cancer and GBM.



A Comparison of SHC1 mRNA expression levels between tumor (TCGA) and normal (GTEx) tissues across pan-cancer after batch effect removal. **B** SHC1 mRNA expression levels in GBM tissues versus normal brain tissues following batch effect correction. **C** Differential analysis of SHC1 protein expression between GBM and adjacent normal tissues in the CPTAC dataset. **D** Genetic alteration frequency of SHC1

across various cancer types from the cBioPortal database. **E** Subcellular localization of SHC1 in U251MG and U2OS cells based on HPA data. **F** Protein-protein interaction (PPI) network displaying SHC1-interacting proteins and their subcellular localizations. *$P < 0.05$, **$P < 0.01$, ***$P < 0.001$, ****$P < 0.0001$; ns, not significant.

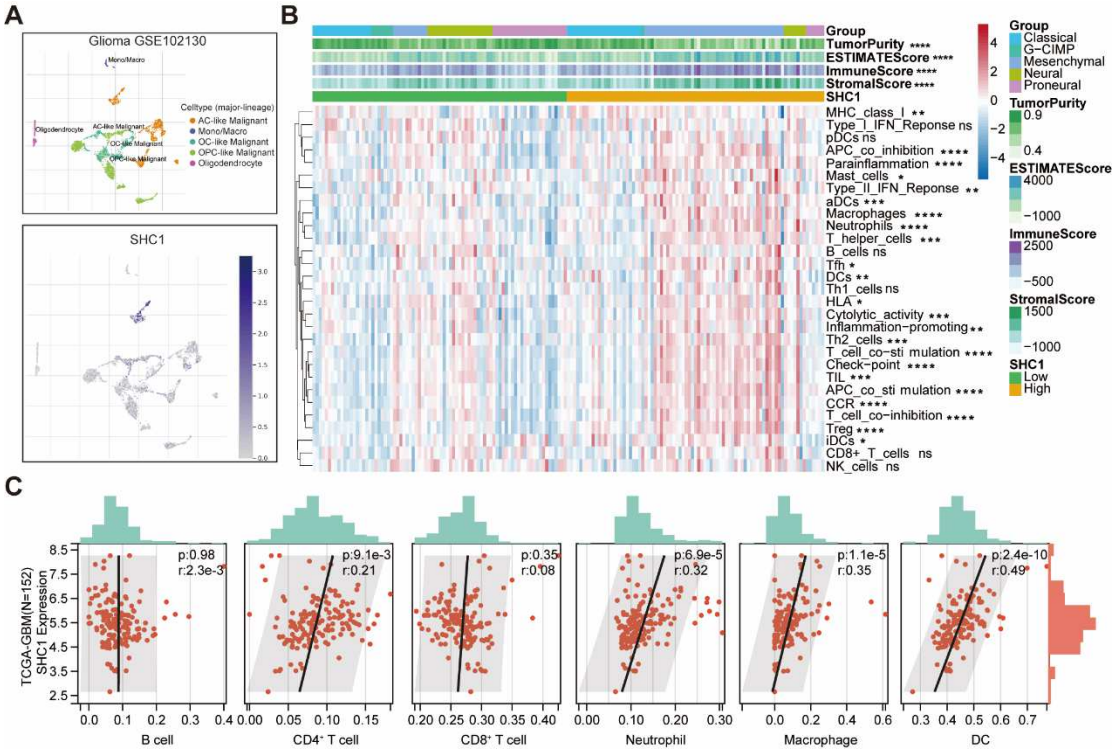
Figure 2. Prognostic value of SHC1 in pan-cancer.



A Summary of associations between SHC1 expression and OS, DSS, DFI, and PFI across cancer types based on univariate Cox regression and Kaplan–Meier analyses. Red indicates SHC1 as a risk factor (HR > 1), while green indicates a protective factor (HR < 1). Only results with $P < 0.05$ are shown. **B** Forest plot summarizing the prognostic role of SHC1 based on OS using univariate Cox regression. Cancer types in which SHC1 serves as a statistically significant risk factor are highlighted in red. **C–F**

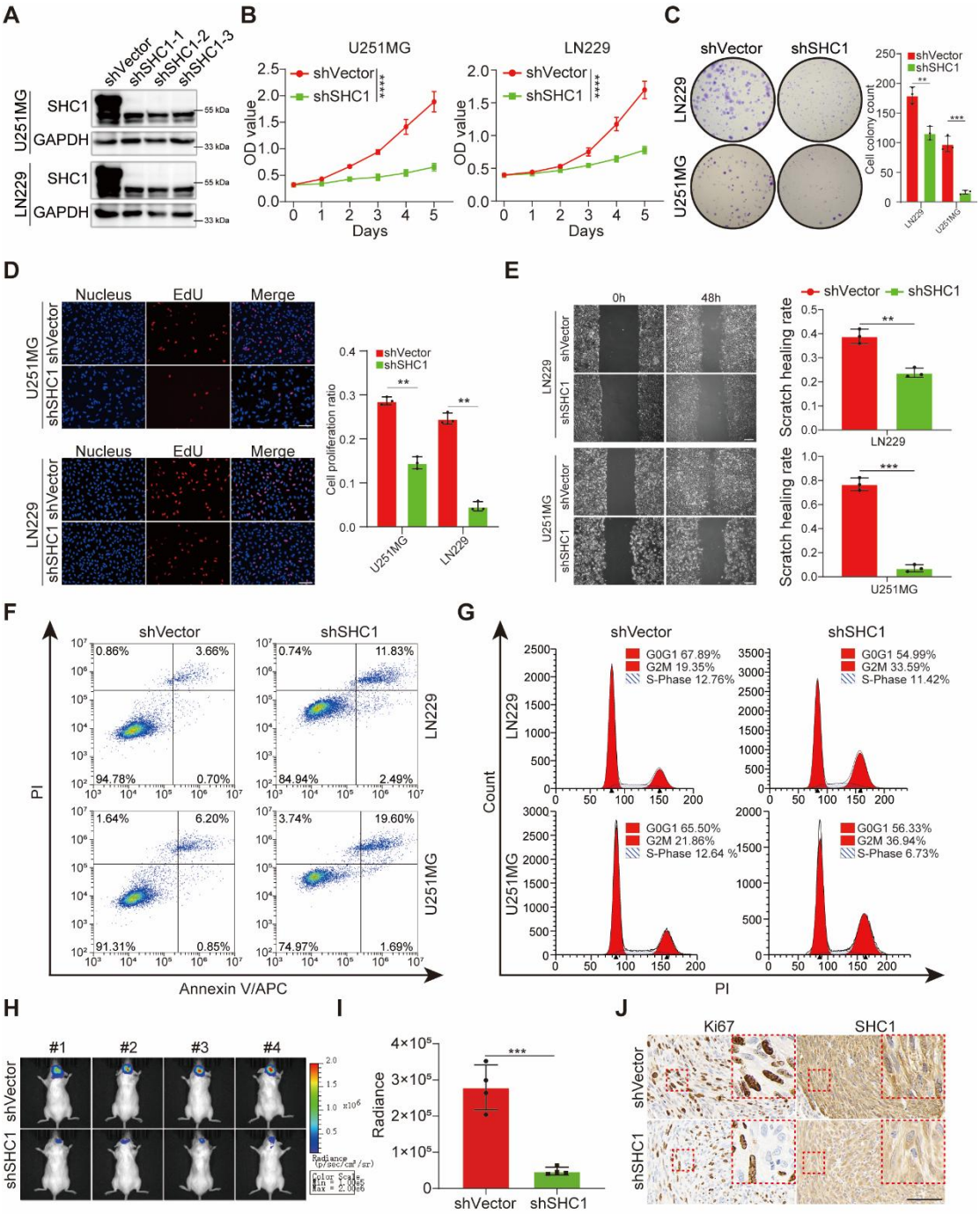
Kaplan–Meier OS curves of SHC1 in GBM (**C**), LGG (**D**), PAAD (**E**), and MESO (**F**).

Figure 3. Immunological landscape of SHC1 in pan-cancer.



A Top: UMAP plot showing the distribution of distinct cell types in the Glioma-GSE102130 dataset. Bottom: UMAP plot depicting SHC1 expression levels across individual cells in the same dataset. **B** Heatmap showing differential enrichment scores of 29 immune-related gene sets and four TME-related scores between SHC1-high and SHC1-low expression groups in GBM. **C** Correlation analysis between SHC1 expression and infiltration levels of various immune cell types in GBM. **P* < 0.05, ***P* < 0.01, ****P* < 0.001, *****P* < 0.0001; ns, not significant.

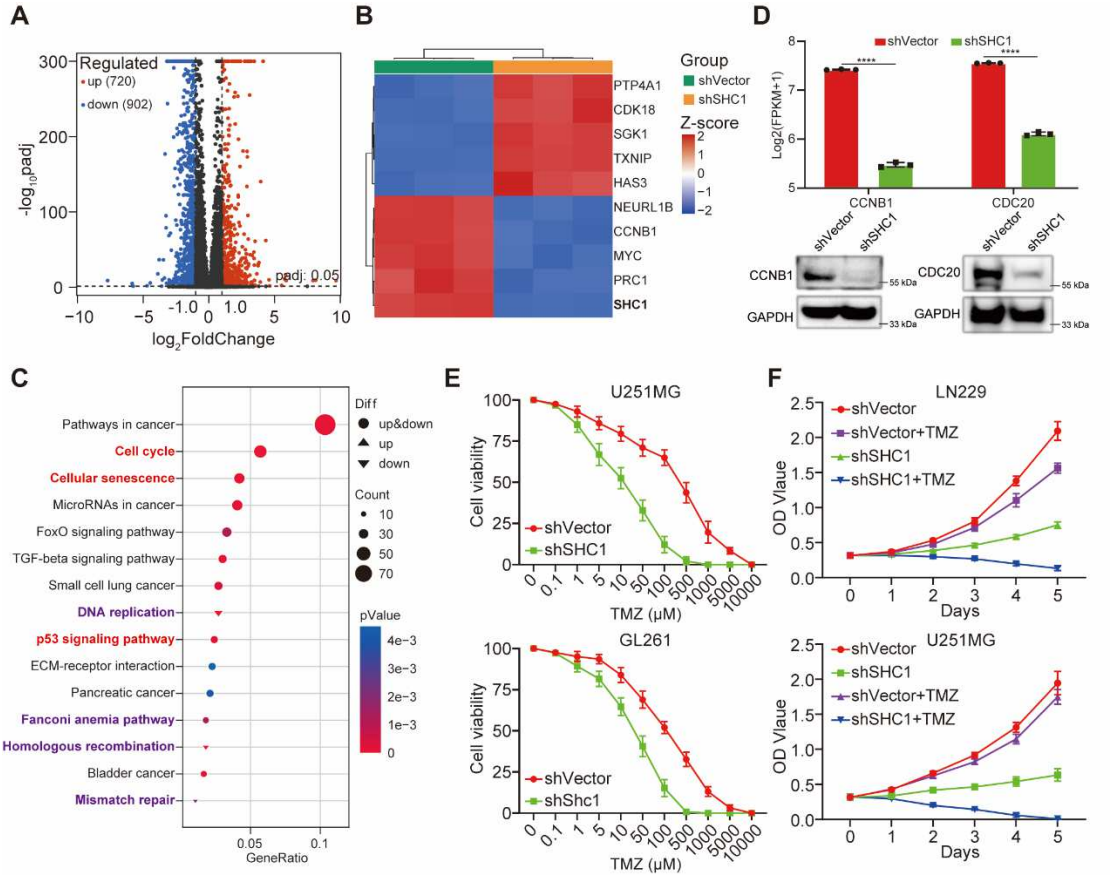
Figure 4. SHC1 knockdown suppresses GBM progression both in vitro and in vivo.



A WB confirming stable and efficient SHC1 knockdown in U251MG and LN229 cells using three independent shRNAs. **B** CCK-8 assay showing that SHC1 knockdown significantly inhibited GBM cell proliferation. **C** Colony formation assay revealing a marked reduction in clonogenic capacity of SHC1-knockdown GBM cells. **D** EdU

incorporation assay indicating a significant reduction in the proportion of proliferating GBM cells after SHC1 knockdown. Scale bar = 100 μm. **E** Wound healing assay showing that directional migration of SHC1-knockdown GBM cells was reduced at 48 h. Scale bar = 100 μm. **F** Flow cytometry analysis revealing a significant increase in apoptotic cell fraction following SHC1 knockdown. **G** Cell cycle analysis demonstrating significant accumulation of SHC1-knockdown GBM cells at the G_2/M phase. **H** Representative IVIS bioluminescence images of intracranial tumors in NCG mice on day 18 post-inoculation with U251-Luc cells stably expressing shVector or shSHC1. **I** Quantification of intracranial bioluminescent signals. **J** IHC staining for Ki-67 in intracranial tumor sections, showing a significant reduction in Ki-67-positive cells in the SHC1-knockdown group. Scale bar = 100 μm. *$P < 0.05$, **$P < 0.01$, ***$P < 0.001$, ****$P < 0.0001$; ns, not significant.

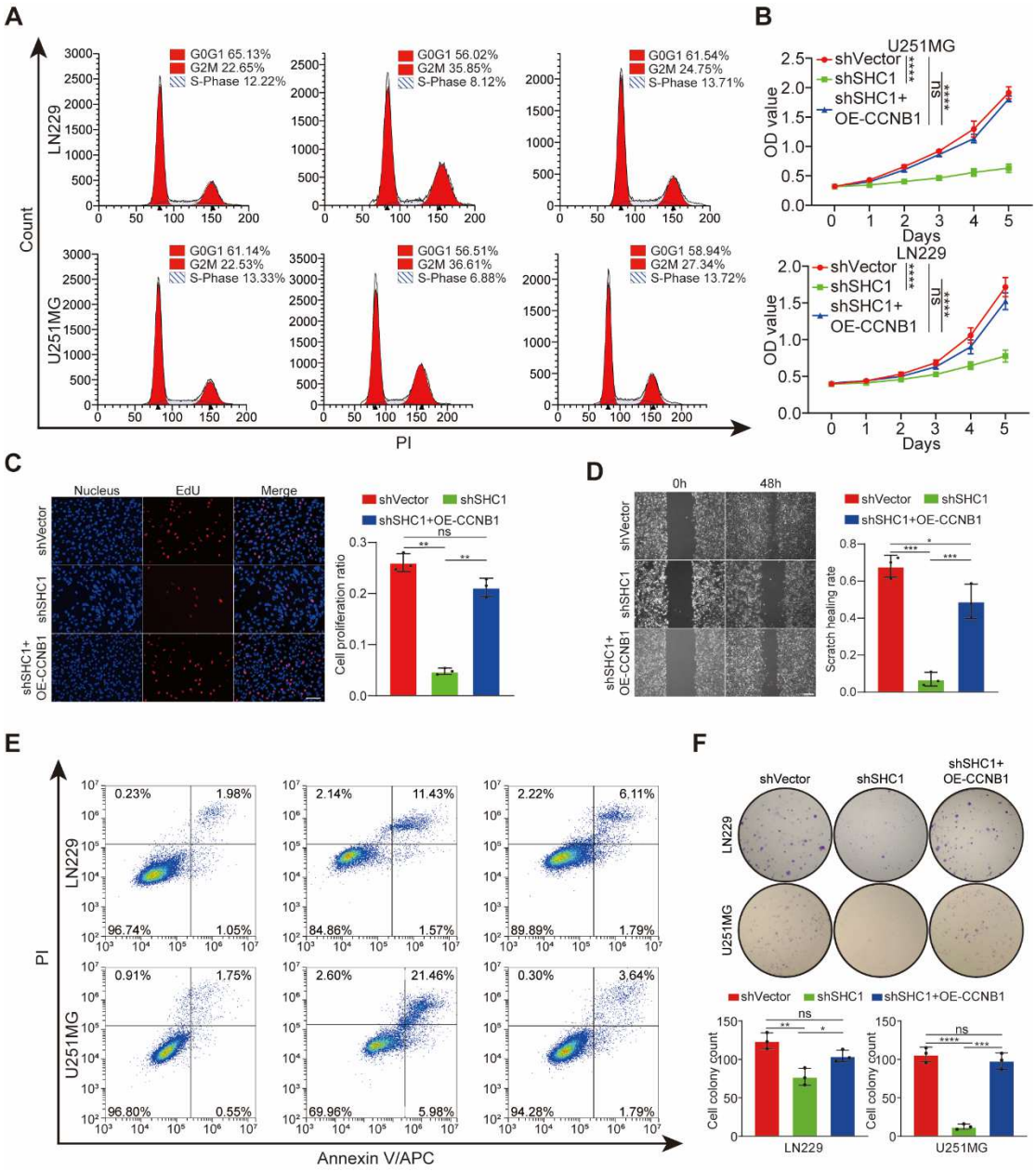
Figure 5. SHC1 regulates cell cycle progression and TMZ chemosensitivity in GBM cells.



A Volcano plot showing DEGs in U251MG cells following SHC1 knockdown. A total of 720 genes were significantly upregulated and 902 genes were downregulated. **B** Heatmap displaying representative upregulated and downregulated genes (selected from top-ranked DEGs) between shVector and shSHC1 groups. **C** KEGG pathway enrichment analysis revealing that SHC1 knockdown-associated DEGs were predominantly enriched in cell cycle- and DNA repair-related pathways. **D** Validation of CCNB1 and CDC20 expression at both mRNA and protein levels in shVector and shSHC1 GBM cells. **E** Cell viability after 48 h of TMZ treatment across different concentrations. **F** Proliferation analysis of GBM cells divided into four groups: shVector, TMZ alone (50 μM), shSHC1 alone, and shSHC1 combined with TMZ (50

μM). ****$P < 0.0001$.

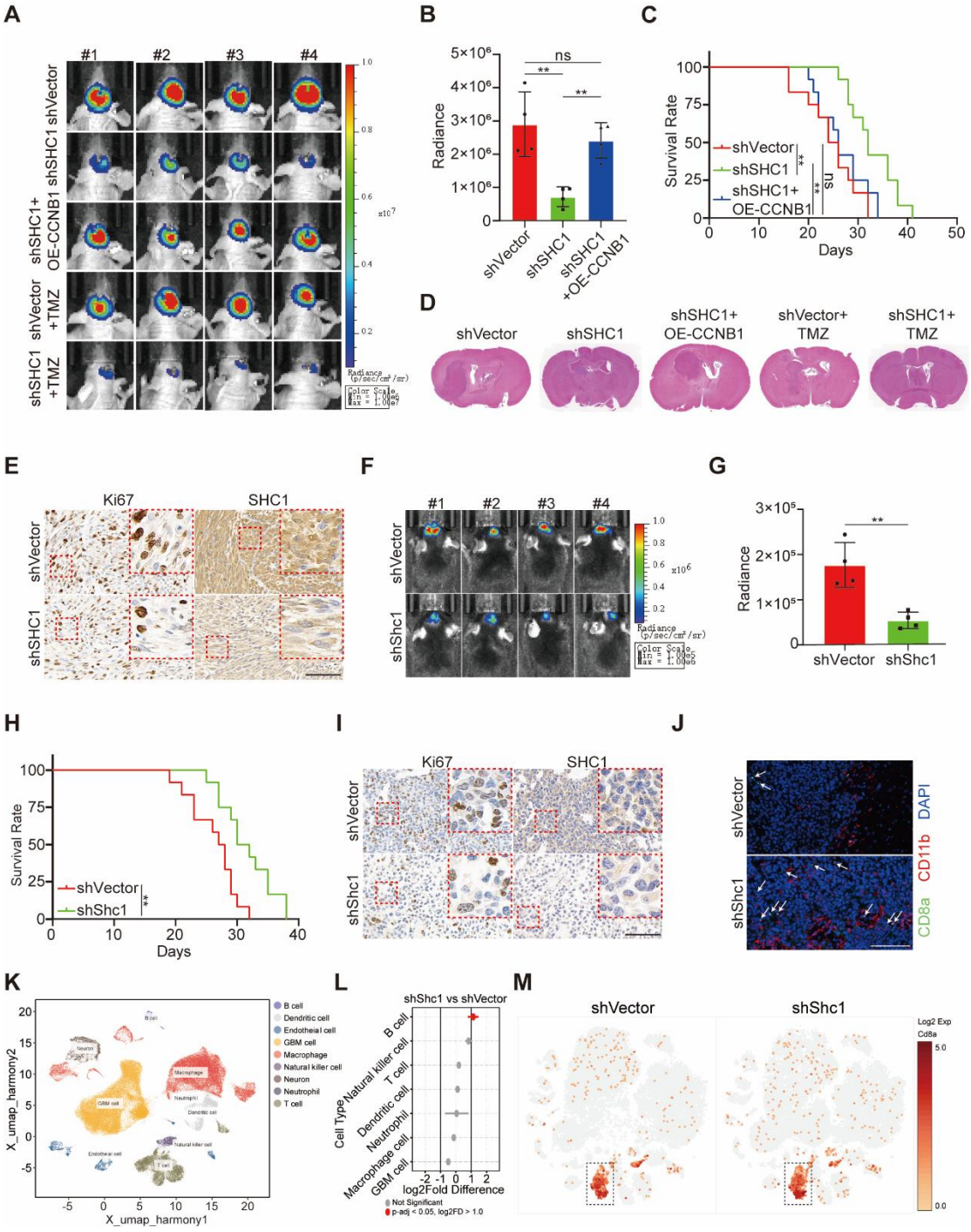
Figure 6. SHC1 knockdown suppresses GBM progression through downregulation of CCNB1.



A Overexpression of CCNB1 in SHC1-knockdown GBM cells significantly reduced the proportion of cells arrested at the G_2/M phase. **B–D** Ectopic CCNB1 expression effectively rescued SHC1 knockdown-induced impairment of cell proliferation (**B**), proliferating cell ratio (**C**), and directional migration (**D**). Scale bar = 100 μm. **E** CCNB1 overexpression significantly reversed SHC1 knockdown-induced apoptosis. **F**

CCNB1 restoration markedly recovered the clonogenic capacity of SHC1-knockdown GBM cells.

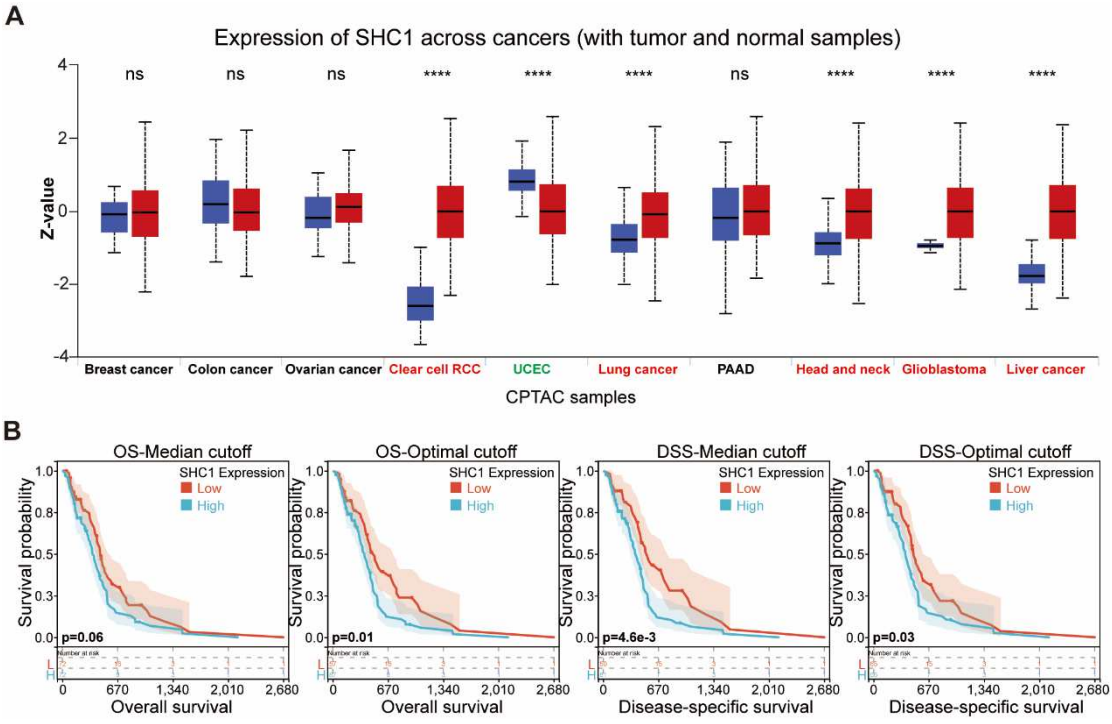
Figure 7. SHC1 knockdown suppresses GBM progression and remodels the immunosuppressive microenvironment in vivo.



A Representative IVIS images of intracranial GBM tumors in nude mice on day 18 post-inoculation across five groups: shVector, shSHC1, shSHC1 + CCNB1, shVector + TMZ, and shSHC1 + TMZ. **B** Quantification of IVIS signals showing that CCNB1

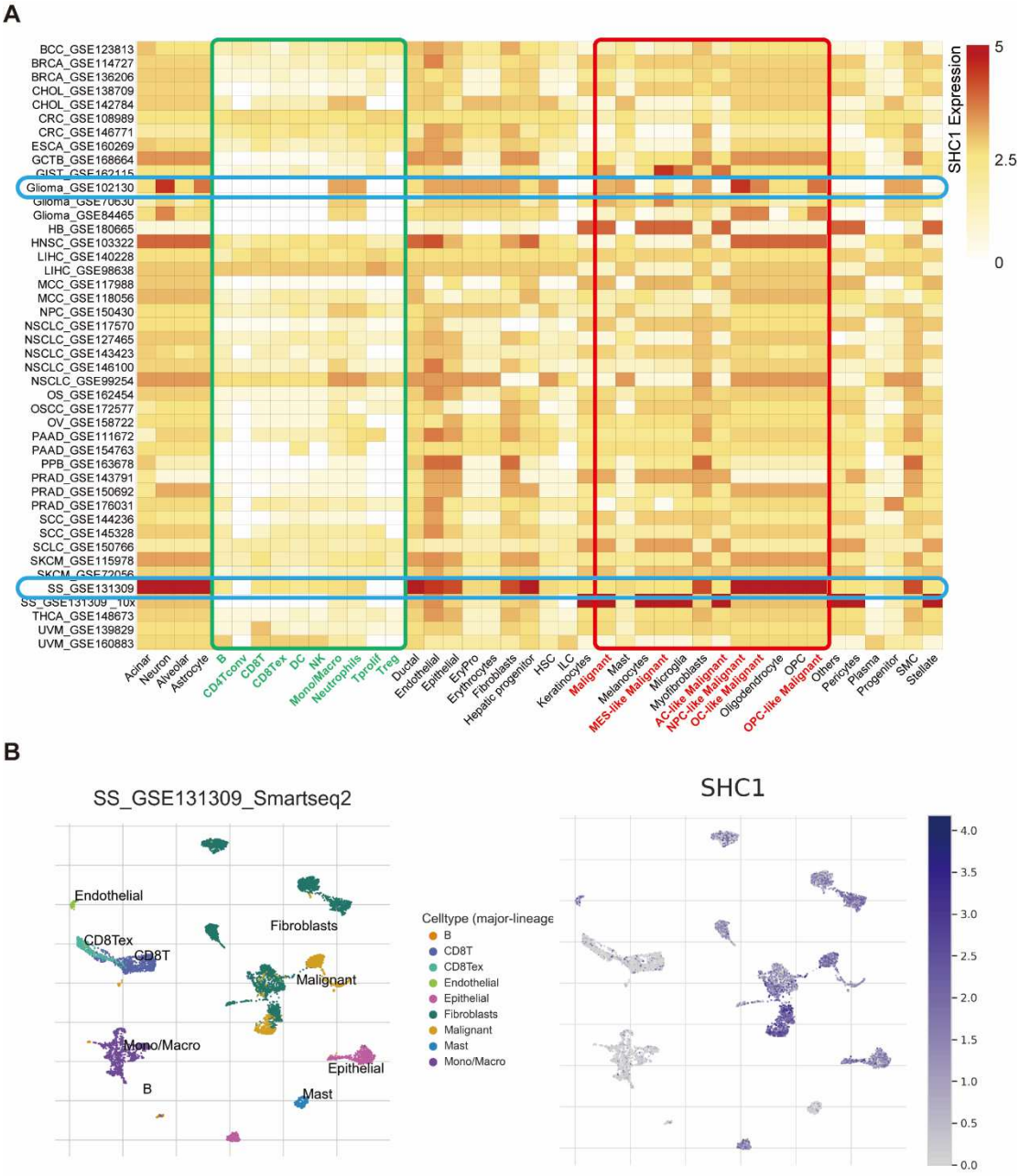
restoration significantly increased intracranial tumor burden. **C** Kaplan–Meier survival analysis demonstrating that SHC1 knockdown significantly prolonged survival of GBM-bearing mice, while CCNB1 overexpression reversed this effect. **D** Representative H&E staining of brain sections from each group (2×). **E** IHC staining for Ki-67 showing reduced Ki-67-positive cells in the shSHC1 group versus control. Scale bar = 100 μm. **F** Representative IVIS images of intracranial GL261-Luc tumors in C57BL/6 mice stably expressing shVector or shShc1, captured on day 18 post-inoculation. **G** Quantification of IVIS signals. **H** Kaplan–Meier survival curves showing that Shc1 knockdown significantly extended survival in C57BL/6 mice. **I** Representative IHC staining and quantitative analysis of Ki-67 in tumor tissues, showing a significantly reduced proportion of Ki-67–positive proliferating cells in the shSHC1 group compared to the control. Scale bar = 100 μm. **J** Immunofluorescence staining of GBM tissue in the brain, scale = 100 μm. **K** UMAP plot showing the distribution of major cell types in mouse intracranial GBM tissues. Cells are colored by annotated cell type. n = 4 control and 4 shShc1 mice.**L** Single-cell RNA-seq analysis of intracranial tumor tissues from shVector and shShc1 groups, showing differential proportions of immune cell subsets between groups. **M** UMAP plots showing the expression of Cd8a in all cells from the shVector (left) and shShc1 (right) groups. Dashed boxes highlight $CD8^+$ cell populations. The numbers of $CD8^+$ cells were 1,109 in the shVector group and 1,982 in the shShc1 group. Color scale indicates Cd8a expression level. $*P < 0.05$, $**P < 0.01$, $***P < 0.001$, $****P < 0.0001$; ns, not significant.

Figure S1. Protein expression of SHC1 in pan-cancer and its prognostic significance in GBM.



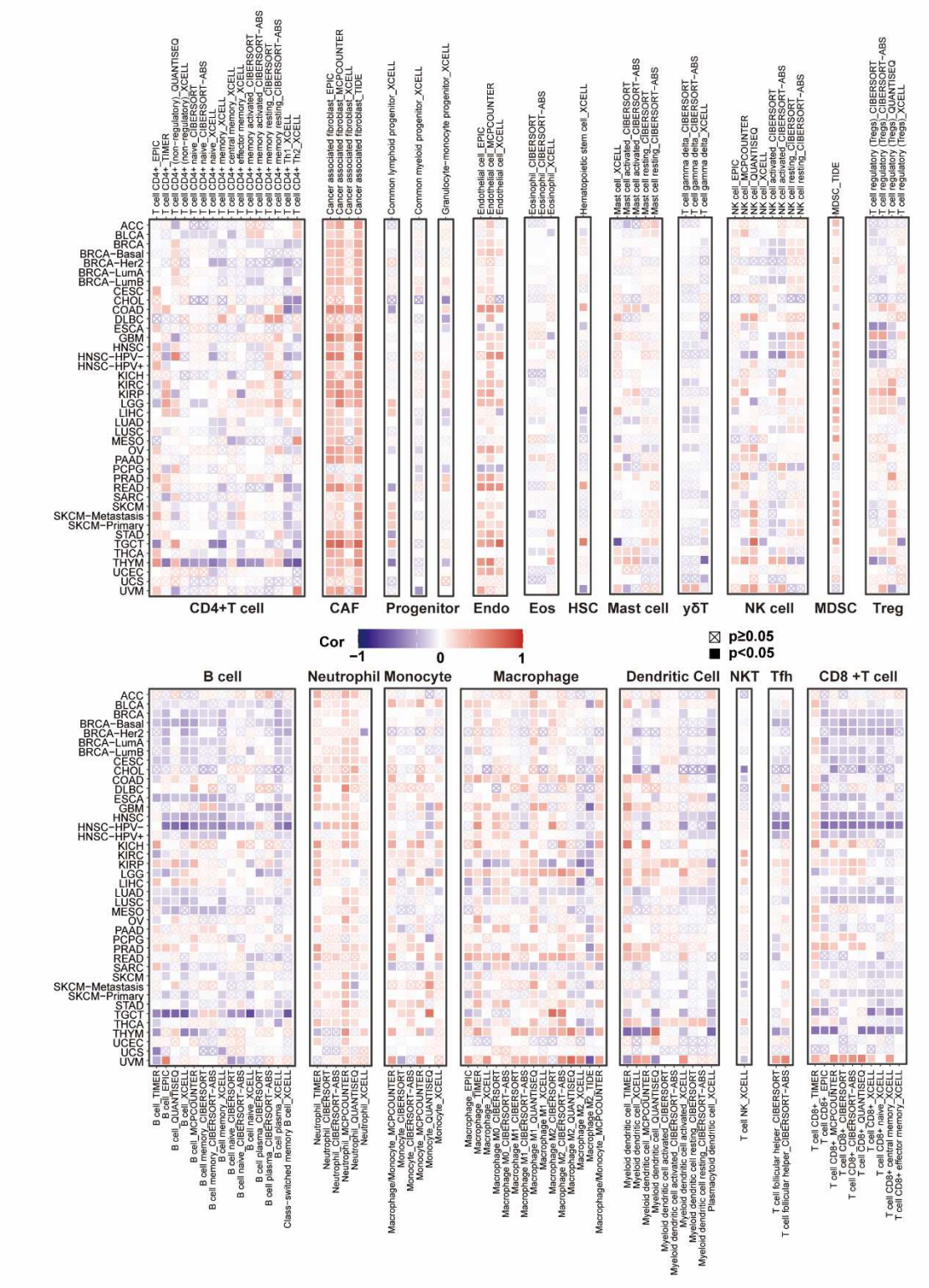
A Differential expression of SHC1 protein between tumor and adjacent normal tissues across cancer types based on the CPTAC dataset. **B** Kaplan–Meier survival curves showing associations between SHC1 expression (stratified by median or optimal cutoff) and OS or DSS in GBM patients. ****$P < 0.0001$; ns, not significant.

Figure S2. SHC1 expression across distinct cell types in tumor tissues.



A Heatmap showing SHC1 expression across different cell types in representative cancer types from the TISCH database. **B** SHC1 expression across distinct cell populations in the SS-GSE131309 dataset.

Figure S3: Correlation of SHC1 expression with immune cell infiltration in pan-cancer.



Heatmap showing correlations between SHC1 expression and infiltration levels of

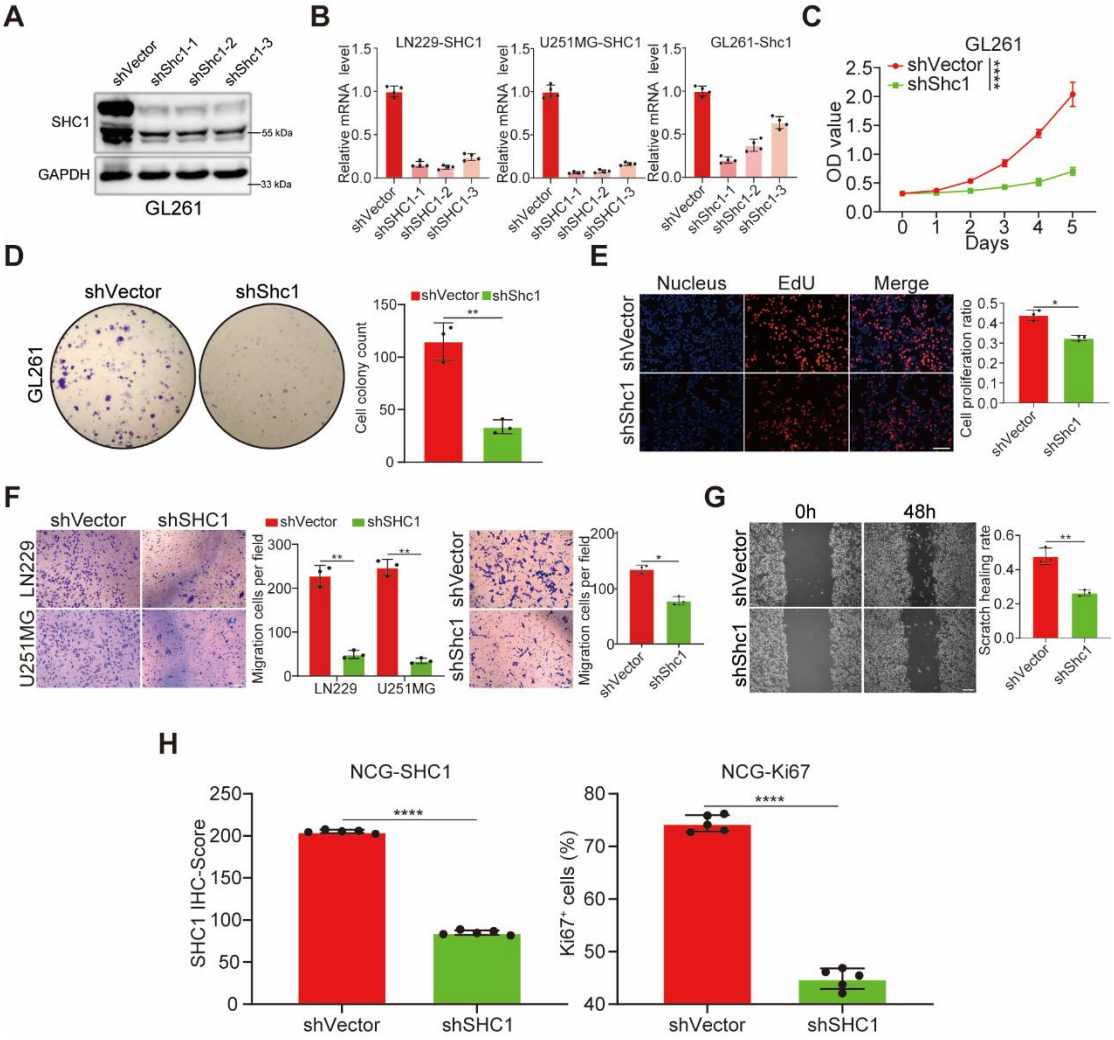
multiple immune cell types across cancers, including $CD4^+$ T cells, γδT cells, NKT cells, Tregs, B cells, neutrophils, monocytes, macrophages, dendritic cells, NK cells, and $CD8^+$ T cells. Red indicates positive correlation; blue indicates negative correlation.

Figure S4: Hallmark GSEA of SHC1 in pan-cancer.



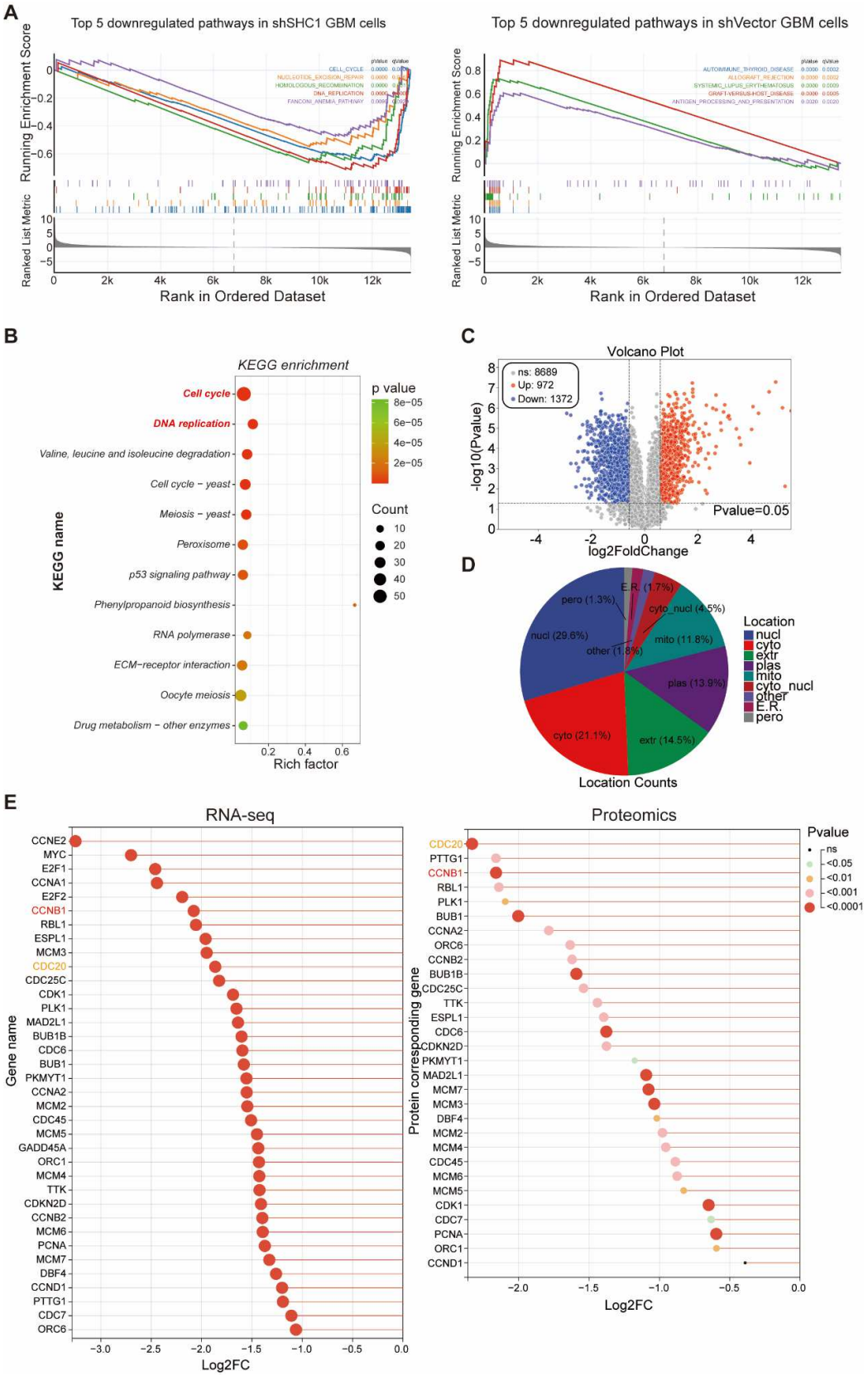
Dot plot depicting enriched Hallmark pathways associated with SHC1 expression across different cancer types. FDR is indicated by circle size; NES is represented by color.

Figure S5. SHC1 knockdown suppresses malignant phenotypes of GBM cells in vitro.



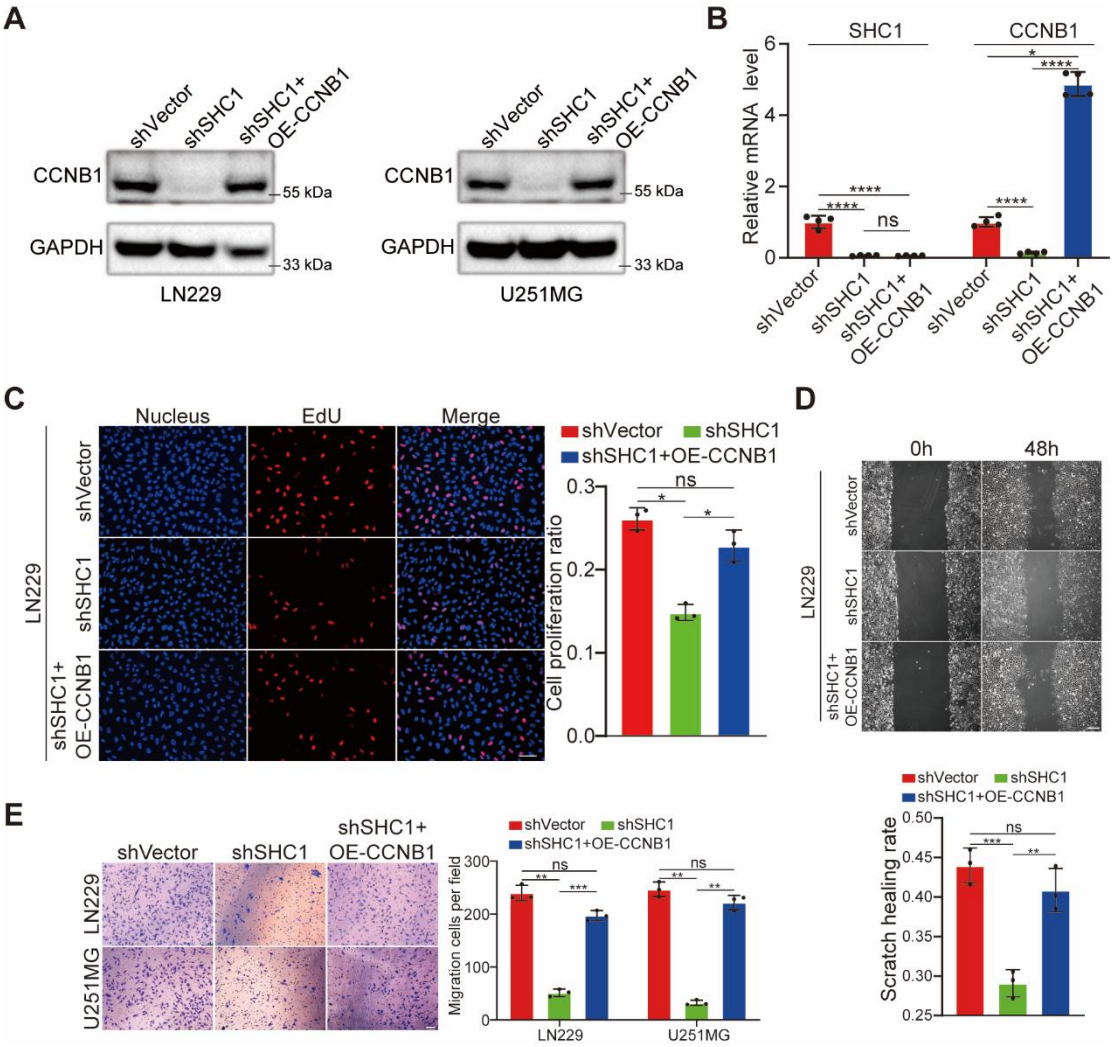
A Western blot confirming efficient SHC1 knockdown in GL261 cells stably expressing shShc1. **B** qRT-PCR validation of SHC1 mRNA levels in U251MG, LN229, and GL261 cells stably expressing shVector or shSHC1/shShc1. **C** CCK-8 assay showing that SHC1 knockdown significantly impaired GL261 cell proliferation. **D–G** SHC1 knockdown markedly reduced colony formation (**D**), proliferating cell ratio (**E**), invasiveness (**F**), and directional migration (**G**) of GL261 cells. Scale bar = 100 μm. **H** IHC quantification of Ki-67-positive cells and SHC1 protein levels in GBM tumors. ****$P < 0.0001$.

Figure S6. Transcriptomic and proteomic profiling of U251MG cells upon SHC1 knockdown.



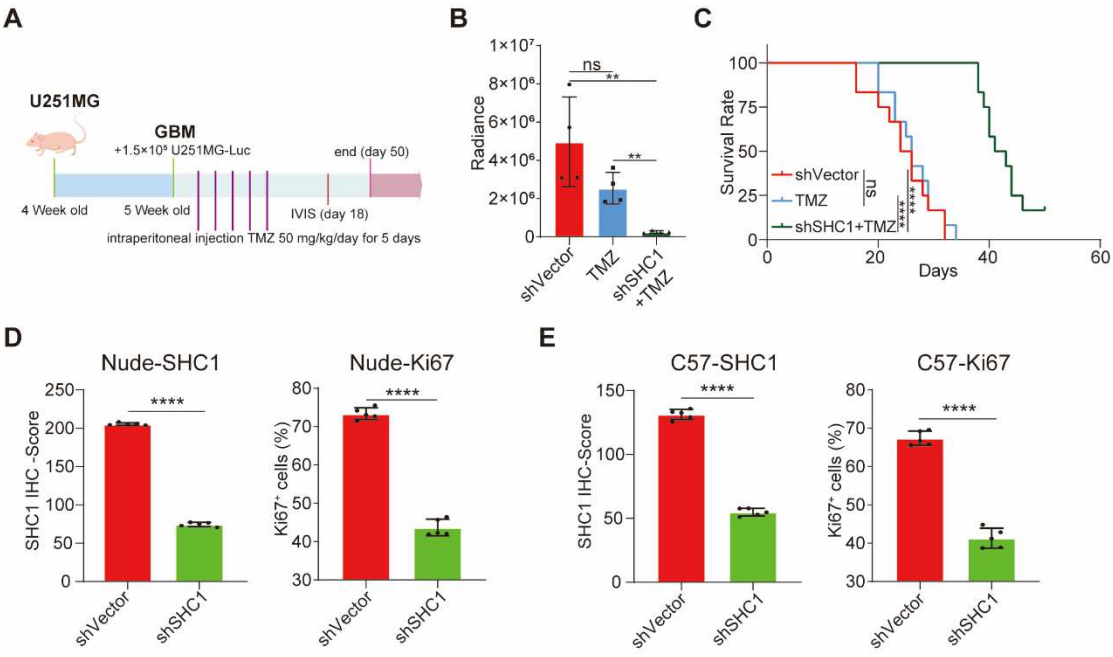
A Top 5 downregulated pathways in shSHC1 versus control cells based on RNA-seq data. **B** KEGG enrichment analysis of DEPs identifying cell cycle and DNA replication as the top enriched pathways. **C** Volcano plot showing DEPs between shSHC1 and control groups, with 972 significantly upregulated and 1,372 downregulated proteins. **D** Subcellular localization distribution of identified DEPs. **E** Integrated analysis of RNA-seq and proteomics data identifying CCNB1 as one of the most significantly and consistently downregulated molecules.

Figure S7. CCNB1 restoration partially reverses SHC1 knockdown-induced growth inhibition in GBM cells.



A Western blot showing that CCNB1 was significantly downregulated upon SHC1 knockdown, and ectopic CCNB1 expression successfully restored its protein level. **B** qRT-PCR confirming that CCNB1 overexpression significantly increased CCNB1 mRNA without affecting SHC1 expression. **C–E** Ectopic CCNB1 expression significantly rescued proliferating cell ratio (**C**), directional migration (**D**), and invasiveness (**E**) of SHC1-knockdown GBM cells.

Figure S8. SHC1 knockdown suppresses intracranial GBM growth and remodels the immunosuppressive microenvironment in vivo.



A The experimental timeline for treating mice with GBM by intraperitoneal injection of TMZ. **B** Quantification of IVIS signals showing that SHC1 knockdown combined with TMZ dramatically reduced intracranial tumor burden. **C** Kaplan–Meier survival curves of C57BL/6 tumor-bearing mice. SHC1 knockdown significantly extended overall survival in combination with TMZ, whereas TMZ monotherapy showed no significant survival benefit. **D** IHC quantification of Ki-67-positive cells and SHC1 protein levels in intracranial GBM tissues from nude mice. **E** IHC quantification of Ki-67-positive cells and SHC1 protein levels in intracranial GBM tissues from C57BL/6 mice.

Supplementary Files

This is a list of supplementary files associated with this preprint. Click to download.

- FigureS1.tif
- FigureS2.tif
- FigureS3.tif
- FigureS4.tif
- FigureS5.tif
- FigureS6.tif
- FigureS7.tif
- FigureS8.tif
- TableS1.xlsx
- TableS2.xlsx